

Mutual Coupling-Aware Channel Estimation and Beamforming for RIS-Assisted Communications

Pinjun Zheng, Simon Tarboush, Hadi Sardeddeen, and Tareq Y. Al-Naffouri

Abstract—This work studies the problems of channel estimation and beamforming for active reconfigurable intelligent surface (RIS)-assisted communication, incorporating the mutual coupling (MC) effect through an electromagnetically consistent model based on scattering parameters. We first demonstrate that MC can be incorporated into a compressed sensing (CS) estimation formulation, albeit with an increase in the dimensionality of the sensing matrix. To overcome this increased complexity, we propose a two-stage strategy. Initially, a low-complexity MC-unaware CS estimation is performed to obtain a coarse channel estimate, which is then used to implement a dictionary reduction (DR) technique, effectively reducing the dimensionality of the sensing matrices. This method achieves low complexity comparable to the conventional MC-unaware approach while providing estimation accuracy close to that of the direct MC-aware CS method. We then consider the joint optimization of RIS configuration and base station (BS) combining in an uplink single-input multiple-output system. We employ an alternating optimization strategy where the BS combiner is derived in closed form for a given RIS configuration. The primary challenge lies in optimizing the RIS configuration, as the MC effect renders the problem non-convex and intractable. To address this, we propose a novel algorithm based on the successive convex approximation (SCA) and the Neumann series. Within the SCA framework, we propose a surrogate function that rigorously satisfies both convexity and equal-gradient conditions to update the iteration direction. Numerical results validate our proposal, demonstrating that the proposed channel estimation and beamforming methods effectively manage the MC in RIS, achieving higher spectral efficiency compared to state-of-the-art approaches.

Index Terms—Mutual coupling, scattering parameter, active reconfigurable intelligent surface, compressed sensing, dictionary reduction, successive convex approximation, Neumann series.

I. INTRODUCTION

Next-generation wireless networks are expected to extend spectral and energy efficiency, peak data rates, and network capacity, necessitating the integration of emerging technologies and game-changing enablers. For example, the quest for abundant contiguous bandwidth drives these networks to shift from conventional sub-6 gigahertz (GHz) frequencies

to higher bands, including upper mid-band [1], millimeter-wave (mmWave) [2], sub-terahertz (THz) [3], and THz [4]. However, higher frequencies present challenges such as increased free space path loss and a higher likelihood of blockage, which limit communication distances and reduce link availability. To mitigate these effects, the integration of reconfigurable intelligent surface (RIS), also known as intelligent reflecting surfaces (IRS) [5], [6], offers a viable solution. RIS technology facilitates real-time, intelligent manipulation of electromagnetic (EM) waves to enhance wireless communication performance [5], [7], while also enabling novel applications [8]–[11].

An RIS is a planar metamaterial-based surface composed of a large number of nearly passive reflecting elements. Various types of RIS have been invented to extend their capability in different scenarios. For example, utilizing reflection-type amplifiers [12], active RIS have been proposed to overcome the limited capacity gains of passive RISs and alleviate the multiplicative fading effect [13]. Additionally, extremely dense and even holographic RISs have gained attention recently for their utmost flexibility and precision in recording and shaping arbitrary-intended EM waves with high energy efficiency [14]–[16]. Although promising, these novel RIS hardware designs introduce new challenges in wireless communications. One of the most pronounced issues is the mutual coupling (MC) effect. Initial investigations indicate that densifying the RIS layout will significantly strengthen the mutual coupling among adjacent RIS unit cells [17], [18]. Furthermore, increasing the RIS amplification coefficients can also substantially exacerbate the impact of MC on channel estimation and localization [19]. Therefore, accurate modeling and sophisticated signal processing for such EM interactions among adjacent RIS unit cells are essential for optimizing performance and maximizing the benefits of such surfaces.

A. Related Work

1) *Conventional RIS Modeling*: The most commonly adopted model for RIS-assisted communication describes the RIS reflection as a linear cascaded channel. That is, the overall channel between transmitter (Tx) and receiver (Rx) is the multiplication of the Tx-RIS subchannel, the RIS reflection response, and the RIS-Rx subchannel [7], [10], [19]. While offering significant mathematical tractability, such linear modeling tacitly assumes that each RIS unit cell radiates EM waves independently, neglecting the nonlinear coupling between these unit cells. Recently, the results in [20] cast doubt on this common linear cascaded model, suggesting it

P. Zheng and S. Tarboush are *co-first authors*; they contributed equally to this paper. P. Zheng and T. Y. Al-Naffouri are with the Electrical and Computer Engineering Program, Division of Computer, Electrical and Mathematical Sciences and Engineering (CEMSE), King Abdullah University of Science and Technology (KAUST), Thuwal, 23955-6900, Kingdom of Saudi Arabia (Email: {pinjun.zheng; tareq.alnaffouri}@kaust.edu.sa). S. Tarboush is an independent researcher from Damascus, Syria (simon.w.tarboush@gmail.com). H. Sardeddeen is with the Electrical and Computer Engineering Department, American University of Beirut (AUB), Lebanon (hadi.sardeddeen@aub.edu.lb).

This work was supported by the KAUST Office of Sponsored Research (OSR) under Award No. ORACRG2021-4695 and the AUB University Research Board.

poorly describes the physical reality. As analyzed in [20], the mutual coupling can result from the proximity-induced coupling due to adjacent radiators, and the reverberation-induced long-range coupling due to environmental scattering multipath. Both mechanisms are characterized by nonlinear interactions. The neglect of proximity-induced coupling becomes untenable when considering densely integrated RIS. Meanwhile, overlooking reverberation-induced long-range coupling presents challenges in rich-scattering environments.

2) *MC-Aware RIS Modeling*: Notable efforts have been dedicated to accurately accounting for mutual coupling in RIS-assisted communications. For instance, based on the first-principles coupled-dipole formalism, a physics-based end-to-end model called PhysFad [21] has been proposed. This model provides a tuning mechanism for jointly modeling transceivers, RIS elements, and the scattering environment. Another suitable theory for modeling mutual coupling is microwave multipoint network theory [22], [23], which extends basic circuit and network concepts to handle complex microwave analyses. Typically, three equivalent representations can be used to analyze microwave networks: impedance, admittance, and scattering parameters [24]. An impedance matrix (Z-parameters) model of MC was first adopted in [17]. Subsequently, equivalent models based on the scattering matrix (S-parameters) have been developed [25]. These models are essentially equivalent and have been unified in, e.g., [24], [26], [27]. From a practical perspective, the scattering matrix model has the advantage of being more directly related to the radiation pattern [28] and verifiable by measurements, as demonstrated in our previous MC measurement work [29].

3) *Channel Estimation*: Considering the sparse channel nature in the mmWave [2] and THz [3], [4] bands, earlier investigations in [30], based on the conventional cascaded model, demonstrated that channel estimation can be formulated as a sparse signal recovery problem, which can be solved using compressed sensing (CS) techniques. In [31] and [32], CS-based channel estimation in multi-user scenarios was formulated and addressed based on the conventional linear model by leveraging double-structured sparsity. Other works such as [33], [34] proposed two-stage channel estimation methods that decouple the cascaded channel into two separate subproblems. However, none of these previous studies account for MC. Moreover, prior information can be incorporated with CS tools to significantly boost the performance on many levels, such as weighted CS algorithms, structured codebook design, and dictionary design as shown in [35]–[37], which has not been investigated for RIS channel estimation problems.

Few works in the literature address the RIS-assisted channel estimation problem with MC. A channel estimation bound evaluation in the presence of MC was conducted in [18]. The results indicate that the closer integration of RIS unit cells will significantly degrade the channel estimation accuracy. Therefore, MC awareness is emerging as a critical concern in designing channel estimators, particularly for systems with densely integrated RIS designs.

4) *Beamforming*: The RIS beamforming based on the conventional linear model has been extensively studied in the literature. Various approaches have been applied

to optimize the RIS phase shifts, such as semidefinite relaxation [38], gradient descent (GD) [39], alternating direction method of multipliers [40], and majorization-minimization [39], [40], among others. More practical designs have also been considered, including dual reflection phase and amplitude variations [41] and designs that account for imperfect channel state information [42]. Additionally, active RIS optimization based on the conventional model has been addressed to improve the sum-rate [43] and to account for hardware impairments [44].

The study of mutual coupling awareness in RIS beamforming is also in its early states. By properly adopting the impedance matrix model accounting for the MC and optimizing the RIS phase shift accordingly, [45] demonstrated an enhanced end-to-end signal-to-noise ratio (SNR), while [46] obtained an improved sum-rate for multi-user interference channels. A joint active and passive beamforming problem was further studied in [28] for a RIS-assisted downlink and uplink transmissions based on the scattering matrix model. Nonetheless, these works do not consider active RISs, which possess a higher amplification factor and will accentuate the MC effect between RIS elements [19]. Additionally, more effective beamforming algorithms are needed for the scattering matrix-based model. For example, some up-to-date works utilize the GD algorithm to optimize the RIS coefficients based on the scattering matrix model [28]. Although decent performance is achieved, the convergence of GD to the global minimum is not always guaranteed in such non-convex problems, which deserves further investigation.

B. Contributions

To the best of the authors' knowledge, this is the first work that comprehensively considers both channel estimation and beamforming for an active RIS-assisted communication in the presence of MC among RIS unit cells. Without loss of generality, we consider an uplink single-input multiple-output (SIMO) communication system assisted by an active RIS. We first formulate and solve the channel estimation problem using the electromagnetic-consistent channel model based on the scattering parameter representation, which takes the RIS MC into account. Based on the estimated channel, we then jointly optimize RIS configuration and base station (BS) combining, again considering the exact MC-aware model. The main contributions of this paper are summarized as follows.

- We formulate and solve the RIS-assisted channel estimation problem in the presence of MC. Specifically, we first demonstrate that the nonlinearity introduced by RIS MC undermines the conventional CS formulation for channel estimation, rendering traditional CS-based estimators infeasible. By carefully manipulating the observation format based on the MC mechanism, we propose a new CS formulation that accounts for MC without any loss of accuracy. Subsequently, we apply the orthogonal matching pursuit (OMP) algorithm [47] to solve the new CS problem. At this stage, similar to [30], we can estimate an equivalent cascaded channel, which is a coupled Kronecker product of the UE-RIS and RIS-BS

subchannels. While the two individual subchannels cannot be separated, we later demonstrate that this equivalent cascaded channel is sufficient for beamforming design.

- We propose a dictionary reduction (DR) strategy to further reduce the complexity of the proposed MC-aware channel estimator by utilizing prior estimation information. While the constructed CS problem accurately accounts for MC, it incurs a dimension lift in the basis space. Specifically, by incorporating MC, the dimension of atoms in the CS dictionary increases from $N_B N_I$ in the conventional solution to $N_B N_I^2$ (here N_B and N_I respectively denote the sizes of the BS and RIS arrays), hindering the feasibility of our method in large-scale RISs. To address this issue, we propose a two-stage strategy to achieve low-complexity yet accurate estimation. This approach first performs the conventional MC-unaware CS estimation to obtain a coarse estimate. Based on this initial estimate, we then design a DR procedure to reduce the dictionary size using the exact MC-aware model. This DR approach can effectively counteract the dimension lift due to the MC effect, achieving complexity comparable to the conventional solution.
- We formulate and solve the joint RIS configuration and BS combiner optimization problem based on the estimated equivalent cascaded channel. To tackle this complex joint optimization problem, we adopt an alternating optimization strategy, optimizing the RIS configuration and BS combiner alternately. For the BS combiner design, a simple closed-form optimal solution is derived. For the RIS configuration optimization, the nonlinear MC mechanism introduces challenges of intractability and non-convexity. We first apply the Neumann series expansion to approximate the objective function and reformulate it as a tractable optimization problem. Since the resultant problem remains non-convex, we adopt the successive convex approximation (SCA) framework to solve it. Based on the SCA principle, we propose a specific surrogate function to obtain the descending direction for iteration. A rigorous proof is provided to demonstrate that this surrogate function satisfies the convexity and equal-gradient conditions within the SCA framework.
- We validate our methods through extensive numerical simulations. In terms of channel estimation accuracy, the proposed estimation method, even with high MC levels, outperforms the *conventional model*-based strategy by several dBs and has a similar accuracy of *exact model*-based procedure but with less complexity (at least 53% reduction). Moreover, the proposed MC-aware joint beamforming algorithm surpasses the state-of-the-art benchmarks, achieving enhanced spectral efficiency.

C. Organization and Notation

The remainder of this paper is organized as follows. Section II introduces the channel model while Section III defines the received signal model and formulates the MC-aware channel estimation problem. Section IV details the proposed low-complexity channel estimation solution. Subsequently,

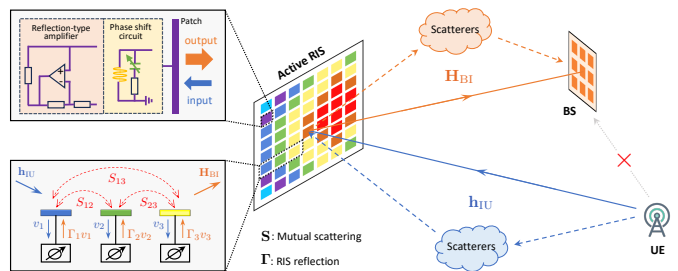


Fig. 1. Illustration of a RIS-assisted uplink SIMO communication system in the presence of MC between RIS unit cells, where the UE-BS direct channel is assumed to be absent.

we define the joint beamforming problem and outline the alternating optimization strategy in Section V. Given that the BS combiner design is addressed with a closed-form solution immediately following the problem definition, we delve into the RIS configuration optimization in Section VI. The simulation results are presented in Section VII, and the conclusion and future directions are given in Section VIII.

We use the following notation throughout the paper. Non-bold lower and upper case letters (e.g., a , A) denote scalars, bold lower case letters (e.g., \mathbf{a}) denote vectors, and bold upper case letters (e.g., \mathbf{A}) denote matrices. We use $A_{i,j}$ to denote the entry at the i^{th} row and j^{th} column of the matrix \mathbf{A} . In addition, $[\mathbf{A}]_{n,:}$ and $[\mathbf{A}]_{:,m}$ denote n^{th} row and m^{th} column of \mathbf{A} , respectively. The superscripts $(\cdot)^{\text{T}}$, $(\cdot)^*$, $(\cdot)^{\text{H}}$, $(\cdot)^{-1}$, and $(\cdot)^{\dagger}$ represent the transpose, conjugate, Hermitian (conjugate transpose), inverse, and pseudo-inverse operators, respectively. For two $M \times N$ matrices \mathbf{A} and \mathbf{B} , $\mathbf{A} \otimes \mathbf{B}$ denotes the $M^2 \times N^2$ Kronecker product matrix. Furthermore, $\mathbf{A} \bullet \mathbf{B}$ denotes the $M^2 \times N$ column-wise Khatri-Rao product matrix, $\mathbf{A} \bullet \mathbf{B} = [[\mathbf{A}]_{:,1} \otimes [\mathbf{B}]_{:,1}, \dots, [\mathbf{A}]_{:,N} \otimes [\mathbf{B}]_{:,N}]$; \odot denotes the Hadamard product.

II. CHANNEL MODEL

Consider an RIS-assisted uplink SIMO communication system,¹ consisting of a single antenna user equipment (UE), an N_B -antenna BS, and an N_I -unit cell RIS, as shown in Fig. 1. To focus on RIS reflection, we assume the UE-BS direct channel does not exist. In this work, the RIS is composed of a uniform planar array (UPA) consisting of $N_I = N_I^h \times N_I^v$ tightly-packed unit cells, where the superscripts h and v denote the horizontal and vertical dimensions, respectively. The same assumption is applied for the BS, i.e., $N_B = N_B^h \times N_B^v$. In the following subsections, we first detail the individual UE-RIS and RIS-BS subchannels, and then elaborate on how the MC between RIS unit cells reshapes the overall cascaded channel.

¹Typically, channel estimation is performed for the uplink channels, and the downlink channels are obtained based on channel reciprocity [32]. Nevertheless, the methodology developed in this paper can also be applied to downlink setups. Although the SIMO setup is used in this work for simplicity, extending the approach to multiple-input multiple-output (MIMO) scenarios is straightforward.

A. The Channel Between UE and RIS

Assuming a far-field propagation scenario, the high-frequency narrow-band frequency-domain channel from the UE to the RIS, $\mathbf{h}_{\text{IU}} \in \mathbb{C}^{N_{\text{I}}}$, is defined as [31]

$$\mathbf{h}_{\text{IU}} = \sqrt{\frac{N_{\text{I}}}{L_{\text{U}}}} \sum_{\ell=1}^{L_{\text{U}}} \alpha_{\ell} \mathbf{a}_{\text{I}}(\phi_{\ell}), \quad (1)$$

where $\alpha_{\ell} \in \mathbb{C}$ denotes the complex channel gain, $\phi_{\ell} \in \mathbb{R}^2$ the angle-of-arrival (AoA) at the RIS, and $\mathbf{a}_{\text{I}}(\phi_{\ell}) \in \mathbb{C}^{N_{\text{I}}}$ the array response vector (ARV) at the RIS corresponding to ϕ_{ℓ} . Note that each AoA (and angle-of-departure (AoD), introduced later) comprises an azimuth and an elevation component, e.g., $\phi_{\ell} = [\phi_{\ell}^{\text{az}}, \phi_{\ell}^{\text{el}}]^{\text{T}}$.² Under a UPA setup, the ARV at the RIS can be expressed as [36]

$$\mathbf{a}_{\text{I}}(\phi_{\ell}) = \frac{1}{\sqrt{N_{\text{I}}}} e^{-j2\pi\phi_{\ell}^{\text{h}} \mathbf{n}(N_{\text{I}}^{\text{h}})} \otimes e^{-j2\pi\phi_{\ell}^{\text{v}} \mathbf{n}(N_{\text{I}}^{\text{v}})}, \quad (2)$$

where $\mathbf{n}(N) = [0, 1, \dots, N-1]^{\text{T}}$, and ϕ_{ℓ}^{h} and ϕ_{ℓ}^{v} are the spatial angles corresponding to the horizontal and vertical dimensions, respectively. Assuming the UPA is deployed on the YZ-plane of the RIS's body coordinate system, we obtain $\phi_{\ell}^{\text{h}} \triangleq d_{\text{I}} \sin(\phi_{\ell}^{\text{az}}) \sin(\phi_{\ell}^{\text{el}}) / \lambda_c$ and $\phi_{\ell}^{\text{v}} \triangleq d_{\text{I}} \cos(\phi_{\ell}^{\text{el}}) / \lambda_c$, where λ_c is the wavelength of the operating frequency, f_c , and d_{I} is the inter-element spacing of the RIS. In addition, L_{U} in (1) is the number of paths between the UE and RIS, where $\ell = 1$ stands for the line-of-sight (LoS) path and $\ell = 2, \dots, L_{\text{U}}$ correspond to $L_{\text{U}} - 1$ non-line-of-sight (NLoS) paths. By concatenating all the ARVs into a matrix form, (1) can be written as [30], [33]

$$\mathbf{h}_{\text{IU}} = \mathbf{A}_{\text{I}}(\phi) \boldsymbol{\sigma}_{\text{IU}}, \quad (3)$$

where we define $\phi = [\phi_1^{\text{T}}, \phi_2^{\text{T}}, \dots, \phi_{L_{\text{U}}}^{\text{T}}]^{\text{T}} \in \mathbb{R}^{2L_{\text{U}}}$, $\mathbf{A}_{\text{I}}(\phi) = [\mathbf{a}_{\text{I}}(\phi_1), \mathbf{a}_{\text{I}}(\phi_2), \dots, \mathbf{a}_{\text{I}}(\phi_{L_{\text{U}}})] \in \mathbb{C}^{N_{\text{I}} \times L_{\text{U}}}$, and $\boldsymbol{\sigma}_{\text{IU}} = \sqrt{N_{\text{I}}/L_{\text{U}}} [\alpha_1, \alpha_2, \dots, \alpha_{L_{\text{U}}}]^{\text{T}} \in \mathbb{C}^{L_{\text{U}}}$ is the beamspace channel vector.

B. The Channel Between RIS and BS

Similarly, the frequency-domain channel from the RIS to the BS, $\mathbf{H}_{\text{BI}} \in \mathbb{C}^{N_{\text{B}} \times N_{\text{I}}}$, can be expressed as [31]

$$\mathbf{H}_{\text{BI}} = \sqrt{\frac{N_{\text{I}} N_{\text{B}}}{L_{\text{B}}}} \sum_{\ell=1}^{L_{\text{B}}} \rho_{\ell} \mathbf{a}_{\text{B}}(\varphi_{\ell}) \mathbf{a}_{\text{I}}^{\text{T}}(\theta_{\ell}), \quad (4)$$

where L_{B} is the number of paths between the RIS and BS, $\rho_{\ell} \in \mathbb{C}$ denotes the complex channel gain, $\varphi_{\ell} \in \mathbb{R}^2$ denotes the AoA at the BS, $\theta_{\ell} \in \mathbb{R}^2$ denotes the AoD at the RIS, and $\mathbf{a}_{\text{B}}(\cdot) \in \mathbb{C}^{N_{\text{B}}}$ and $\mathbf{a}_{\text{I}}(\cdot) \in \mathbb{C}^{N_{\text{I}}}$ denote the ARVs of the antenna arrays at the BS and RIS, respectively. We denote d_{B} as the inter-element spacing of the BS. Analogously, by concatenating all the BS/RIS ARVs and the channel coefficients in a matrix form, the channel \mathbf{H}_{BI} can be equivalently written as [30], [33]

$$\mathbf{H}_{\text{BI}} = \mathbf{A}_{\text{B}}(\varphi) \boldsymbol{\Sigma}_{\text{BI}} \mathbf{A}_{\text{I}}^{\text{T}}(\theta), \quad (5)$$

²We define the elevation angle as the angle between the direction of interest and the positive Z-axis, which is also called the inclination angle.

where we define the angle vectors $\varphi = [\varphi_1^{\text{T}}, \varphi_2^{\text{T}}, \dots, \varphi_{L_{\text{B}}}^{\text{T}}]^{\text{T}} \in \mathbb{R}^{2L_{\text{B}}}$, $\theta = [\theta_1^{\text{T}}, \theta_2^{\text{T}}, \dots, \theta_{L_{\text{B}}}^{\text{T}}]^{\text{T}} \in \mathbb{R}^{2L_{\text{B}}}$, the array response matrices $\mathbf{A}_{\text{B}}(\varphi) = [\mathbf{a}_{\text{B}}(\varphi_1), \mathbf{a}_{\text{B}}(\varphi_2), \dots, \mathbf{a}_{\text{B}}(\varphi_{L_{\text{B}}})] \in \mathbb{C}^{N_{\text{B}} \times L_{\text{B}}}$, $\mathbf{A}_{\text{I}}(\theta) = [\mathbf{a}_{\text{I}}(\theta_1), \mathbf{a}_{\text{I}}(\theta_2), \dots, \mathbf{a}_{\text{I}}(\theta_{L_{\text{B}}})] \in \mathbb{C}^{N_{\text{I}} \times L_{\text{B}}}$, and the beamspace channel matrix $\boldsymbol{\Sigma}_{\text{BI}} = \sqrt{N_{\text{B}} N_{\text{I}} / L_{\text{B}}} \text{diag}(\rho_1, \rho_2, \dots, \rho_{L_{\text{B}}}) \in \mathbb{C}^{L_{\text{B}} \times L_{\text{B}}}$.

C. Conventional Cascaded Channel Model

Since we have assumed the UE-BS direct link to be absent, the conventional RIS-assisted channel model—without accounting for mutual coupling between RIS unit cells—can be written as [7], [9], [10], [19], [30], [32], [33]

$$\mathbf{h}_{\text{cv}} = \mathbf{H}_{\text{BI}} \boldsymbol{\Gamma} \mathbf{h}_{\text{IU}}, \quad (6)$$

where $\boldsymbol{\Gamma} = \text{diag}(\boldsymbol{\gamma})$, and $\boldsymbol{\gamma} \in \mathbb{C}^{N_{\text{I}}}$ is the vector of RIS reflection coefficients. The reflection coefficient of the i^{th} RIS unit cell can be expressed as $\gamma_i = a_i e^{j\vartheta_i}$, where $a_i \in \mathbb{R}^+$ represents the amplification factor and $\vartheta_i \in (0, 2\pi)$ denotes the phase shift. Both a_i and ϑ_i are reconfigurable; however, they are usually dependent on each other [48]. For nearly-passive RISs, $a_i \in (0, 1]$, as RISs passively reflect signals without power amplification. When reflection-type amplifiers are incorporated, which is known as active RISs, signal amplification is enabled and $a_i > 1$ is available [12], [13], [49]. It has been shown in [19] that a higher amplification factor of RIS accentuates the impact of mutual coupling between RIS unit cells. Hence, this work employs the active RIS setup to comprehensively evaluate its impact under MC and propose the corresponding solutions.

By examining (6), it is evident that the received signal at the BS is a linear combination of signals reflected from each RIS unit cell. This model assumes that each RIS unit cell reflects incident EM waves independently without any interaction, thereby neglecting the MC effect. In scenarios where strong MC exists among RIS unit cells, this assumption can lead to significant model mismatch and pose challenges for applications such as channel estimation [18], ultimately degrading overall communication performance.

D. Mutual Coupling-Aware Channel Model

Although the MC effect is sufficiently weak and can be reasonably omitted in many cases, recent studies have shown that the MC effect between RIS unit cells is pronounced when they are tightly integrated (e.g. holographic RIS/MIMO [14]–[16]) or the amplification factor increases (e.g., active RISs [19], [49]). Based on the S-parameter multiport network theory, a mutual coupling-aware communication model has been recently derived and validated [25], [26], [29], which will be adopted in this paper. To focus on the RIS, this work neglects the mutual coupling at the BS.

By incorporating the mutual coupling effect within the RIS response, the channel model (6) is reformulated as [25]–[29]

$$\mathbf{h}_{\text{mc}} = \mathbf{H}_{\text{BI}} (\boldsymbol{\Gamma}^{-1} - \mathbf{S})^{-1} \mathbf{h}_{\text{IU}}, \quad (7)$$

where $\mathbf{S} \in \mathbb{C}^{N_{\text{I}} \times N_{\text{I}}}$ is the scattering matrix within the RIS unit cells, characterizing the mutual coupling effect. Specif-

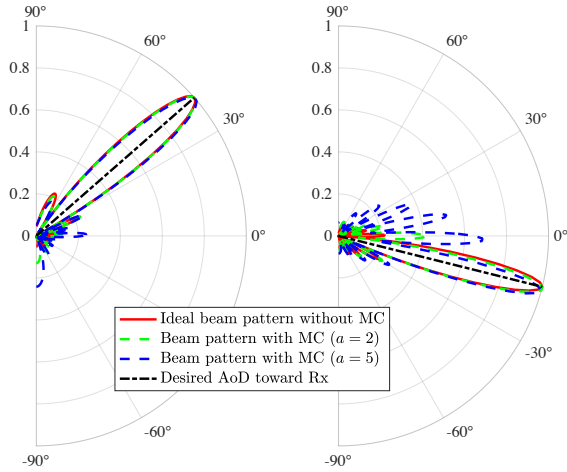


Fig. 2. Normalized beam pattern of the RIS reflection using the directional beam $\gamma = a\mathbf{a}_1^*(\theta) \odot \mathbf{a}_1^*(\phi)$ in a 16-element ULA layout RIS. Here, we test over different values of the RIS amplification factor $a = \{2, 5\}$, assuming all unit cells maintain the same amplification factor. The scattering matrix \mathbf{S} is assigned based on the measured data in [29].

ically, $S_{i,j}$ denotes the scattering parameter between the i^{th} and j^{th} unit cells of the RIS, which is defined as [22]

$$S_{i,j} = \frac{V_i^{\text{out}}}{V_j^{\text{in}}} \Big|_{V_k^{\text{in}}=0, \forall k \neq j}, \quad (8)$$

where V_j^{in} denotes the voltage wave driving at the j^{th} unit cell and V_i^{out} denotes the voltage wave coming out from the i^{th} unit cell. The initial derivation of model (7) can be found in [50], with the complete derivation and analysis available in, e.g., [24], [26], [27]. Additionally, an experimental validation of (7) on a real RIS prototype has been reported in [29]. For clarity, we refer to (6) as the *conventional model* and (7) as the *exact model*. Note that by setting $\mathbf{S} = \mathbf{0}$, the exact model reduces to the conventional model.

Remark 1: It can be inferred from (7) that with the same level of MC, higher amplification of the RIS can exacerbate the impact of MC. This is because the scattering matrix \mathbf{S} is superposed on the inversion of $\mathbf{\Gamma}$. Hence, the greater the values in $\mathbf{\Gamma}$, the more significantly its inversion can be impacted by \mathbf{S} .

To verify the inference in Remark 1, Fig. 2 depicts the normalized beam pattern reflected from RIS when a directional beam $\gamma = a\mathbf{a}_1^*(\theta) \odot \mathbf{a}_1^*(\phi)$ is used in the RIS. This evaluation is based on the real measured mutual scattering parameters provided in [29]. As illustrated, when the RIS amplification is low ($a = 2$), the impact of MC on the RIS radiation pattern is weak. However, when the RIS amplification is enlarged ($a = 5$), we observe that the same MC can more significantly distort the beam pattern. Furthermore, we also observe that the severity of the impact of MC varies across different AoDs, meaning that the impact of MC is direction-selective. Nevertheless, the principle revealed in Remark 1 holds across different directions.

III. SIGNAL MODEL AND CS FORMULATION

A. The Received Signal

For illustrative convenience, this work assumes that the BS is equipped with a single radio frequency chain (RFC)

and employs a fully digital beamforming scheme.³ We start the training procedure by sending pilots—through the uplink channel—using M_I random RIS configurations $\gamma_{m_I} \in \mathbb{C}^{N_I}$ (equivalently $\mathbf{\Gamma}_{m_I} = \text{diag}(\gamma_{m_I})$), $m_I = 1, 2, \dots, M_I$. For each RIS configuration, the BS records M_B received pilots through random combining weights $\mathbf{w}_{m_B} \in \mathbb{C}^{N_B}$, $m_B = 1, 2, \dots, M_B$. Thus, the number of total training measurements is $M_B M_I$. Based on the exact model (7), the received signal for the (m_B, m_I) measurements is given by⁴

$$y_{m_B, m_I} = \mathbf{w}_{m_B}^H \mathbf{H}_{\text{BI}} (\mathbf{\Gamma}_{m_I}^{-1} - \mathbf{S})^{-1} \mathbf{h}_{\text{IU}} x_{m_I} + \omega_{m_B, m_I}, \quad (9)$$

where x_{m_I} is the transmitted training pilot and ω_{m_B, m_I} denotes the total additive noise. Here, we assume $\mathbb{E}[x_{m_I} x_{m_I}^H] = P_U$, where P_U is the total UE power used per transmission during the training phase. Based on the propagation model of active RISs, the total noise ω_{m_B, m_I} can be expressed as [13], [49]

$$\omega_{m_B, m_I} = \mathbf{w}_{m_B}^H (\mathbf{H}_{\text{BI}} (\mathbf{\Gamma}_{m_I}^{-1} - \mathbf{S})^{-1} \boldsymbol{\omega}_{m_B, m_I}^{\text{I}} + \boldsymbol{\omega}_{m_B, m_I}^{\text{B}}), \quad (10)$$

where $\boldsymbol{\omega}_{m_B, m_I}^{\text{I}} \sim \mathcal{CN}(\mathbf{0}, \sigma_{\text{I}}^2 \mathbf{I}_{N_I})$ is the thermal noise at the active RIS and $\boldsymbol{\omega}_{m_B, m_I}^{\text{B}} \sim \mathcal{CN}(\mathbf{0}, \sigma_{\text{B}}^2 \mathbf{I}_{N_B})$ is the thermal noise at the BS.

We denote the matrix of the resultant received signals after taking away the impact of x_{m_I} using a matched filter [36], [37] as $\mathbf{Y} \in \mathbb{C}^{M_B \times M_I}$, which is given by

$$[\mathbf{Y}]_{:, m_I} = \sqrt{P_U} \mathbf{W}^H \mathbf{H}_{\text{BI}} (\mathbf{\Gamma}_{m_I}^{-1} - \mathbf{S})^{-1} \mathbf{h}_{\text{IU}} + \bar{\boldsymbol{\omega}}_{m_I}, \quad (11)$$

where $\mathbf{W} = [\mathbf{w}_1, \mathbf{w}_2, \dots, \mathbf{w}_{M_B}] \in \mathbb{C}^{N_B \times M_B}$ and $\bar{\boldsymbol{\omega}}_{m_I} = [\omega_{1, m_I}, \omega_{2, m_I}, \dots, \omega_{M_B, m_I}]^T \in \mathbb{C}^{M_B}$.

In the following subsections, we present some useful mathematical transformations based on the nature of the received signals to reveal a CS-like structure, thereby facilitating the later development of the channel estimation method. We first recap the conventional formulation without MC, and then propose a new formulation that accurately accounts for MC.

B. The CS Formulation Based on the Conventional Model

Based on the conventional model that does not account for MC, one can rewrite (11) as

$$[\mathbf{Y}_{\text{cv}}]_{:, m_I} \stackrel{(a)}{=} \sqrt{P_U} \mathbf{W}^H \mathbf{H}_{\text{BI}} \mathbf{\Gamma}_{m_I} \mathbf{h}_{\text{IU}} + \bar{\boldsymbol{\omega}}_{m_I}, \quad (12)$$

$$\stackrel{(b)}{=} \sqrt{P_U} \mathbf{W}^H \mathbf{H}_{\text{BI}} \text{diag}(\mathbf{h}_{\text{IU}}) \gamma_{m_I} + \bar{\boldsymbol{\omega}}_{m_I}, \quad (13)$$

where step (a) can be obtained from (11) by setting $\mathbf{S} = \mathbf{0}$ as mentioned in Section II-D, and step (b) is justified by the fact that $\mathbf{\Gamma}_{m_I} = \text{diag}(\gamma_{m_I})$. Here, we denote the received signal based on the conventional model as \mathbf{Y}_{cv} to distinguish it from the exact received signal \mathbf{Y} defined in (11). Furthermore, we define the *conventional equivalent cascaded channel* as [30]

$$\mathbf{G}_{\text{cv}} \triangleq \mathbf{H}_{\text{BI}} \text{diag}(\mathbf{h}_{\text{IU}}). \quad (14)$$

Based on (13) and (14), we have the following observation model [7], [30], [31]

$$\mathbf{Y}_{\text{cv}} = \sqrt{P_U} \mathbf{W}^H \mathbf{G}_{\text{cv}} \boldsymbol{\Theta}_{\text{cv}} + \boldsymbol{\Omega}, \quad (15)$$

³Although this assumption is made, the methodology developed in this paper can be easily adapted to fit the analog/hybrid beamforming system.

⁴We assume that the number of transmitted pilots is equal to the total number of RIS configurations, which is M_I . Moreover, each transmitted pilot by the UE corresponds to one configuration of the RIS.

where $\Theta_{cv} \triangleq [\gamma_1, \gamma_2, \dots, \gamma_{M_I}] \in \mathbb{C}^{N_I \times M_I}$ and $\Omega \triangleq [\bar{\omega}_1, \bar{\omega}_2, \dots, \bar{\omega}_{M_I}] \in \mathbb{C}^{M_B \times M_I}$. Then, we vectorize \mathbf{Y}_{cv} as

$$\text{vec}(\mathbf{Y}_{cv} - \Omega) = \sqrt{P_U} (\Theta_{cv}^T \otimes \mathbf{W}^H) \text{vec}(\mathbf{G}_{cv}). \quad (16)$$

According to (3), (5), and (14), we can further express the $\text{vec}(\mathbf{G}_{cv})$ term as

$$\begin{aligned} \text{vec}(\mathbf{G}_{cv}) &= \text{vec}(\mathbf{H}_{BI} \text{diag}(\mathbf{h}_{IU})) = \text{vec}(\mathbf{H}_{BI} \bullet \mathbf{h}_{IU}^T) \\ &= \text{vec}((\mathbf{A}_B(\varphi) \Sigma_{BI} \mathbf{A}_I^T(\theta)) \bullet (\sigma_{IU}^T \mathbf{A}_I^T(\phi))) \\ &= \text{vec}((\mathbf{A}_B(\varphi) \Sigma_{BI} \otimes \sigma_{IU}^T) (\mathbf{A}_I^T(\theta) \bullet \mathbf{A}_I^T(\phi))) \\ &= \text{vec}((\mathbf{A}_B(\varphi) \otimes 1) (\Sigma_{BI} \otimes \sigma_{IU}^T) (\mathbf{A}_I^T(\theta) \bullet \mathbf{A}_I^T(\phi))) \\ &= \text{vec}(\mathbf{A}_B(\varphi) (\Sigma_{BI} \otimes \sigma_{IU}^T) (\mathbf{A}_I^T(\theta) \bullet \mathbf{A}_I^T(\phi))) \\ &= \underbrace{\left((\mathbf{A}_I^T(\theta) \bullet \mathbf{A}_I^T(\phi))^T \otimes \mathbf{A}_B(\varphi) \right)}_{\mathbf{D}_{cv}} \text{vec}(\Sigma_{BI} \otimes \sigma_{IU}^T). \end{aligned} \quad (17)$$

By substituting (17) into (16), we obtain

$$\text{vec}(\mathbf{Y}_{cv} - \Omega) = \sqrt{P_U} \Psi_{cv} \mathbf{D}_{cv} \text{vec}(\Sigma_{BI} \otimes \sigma_{IU}^T), \quad (18)$$

where we define $\Psi_{cv} \triangleq \Theta_{cv}^T \otimes \mathbf{W}^H \in \mathbb{C}^{M_B M_I \times N_B N_I}$ as the known measurement matrix, and \mathbf{D}_{cv} is the basis matrix. Here, it is clear that (18) is a typical CS problem structure [51]. By carefully designing the dictionary on \mathbf{D}_{cv} and adopting sparse CS estimation algorithms, we can recover the equivalent cascaded channel \mathbf{G}_{cv} based on the received signal \mathbf{Y}_{cv} , since $\text{vec}(\mathbf{G}_{cv}) = \mathbf{D}_{cv} \text{vec}(\Sigma_{BI} \otimes \sigma_{IU}^T)$.

C. The CS Formulation Based on the Exact Model

Now let's consider the case with MC. Due to the existence of matrix \mathbf{S} , the RIS response $(\Gamma_{m_I}^{-1} - \mathbf{S})^{-1}$ is no longer a diagonal matrix. Consequently, the step (b) in (13) becomes invalid. Especially in cases with strong MC, neglecting this factor can result in significant model mismatch and lead to the failure of channel estimation. The following derivation aims to formulate an accurate CS structure accounting for MC.

For notational convenience, we denote $\bar{\Gamma}_{m_I} \triangleq (\Gamma_{m_I}^{-1} - \mathbf{S})^{-1}$ and $\xi_{m_I} \triangleq \text{vec}(\bar{\Gamma}_{m_I}) \in \mathbb{C}^{N_I^2}$. Utilizing (3) and (5), we can express (11) as

$$\begin{aligned} ([\mathbf{Y}]_{:,m_I} - \bar{\omega}_{m_I}) / \sqrt{P_U} &= \mathbf{W}^H \mathbf{H}_{BI} (\Gamma_{m_I}^{-1} - \mathbf{S})^{-1} \mathbf{h}_{IU} \\ &= \text{vec}(\mathbf{W}^H \mathbf{A}_B(\varphi) \Sigma_{BI} \mathbf{A}_I^T(\theta) \bar{\Gamma}_{m_I} \mathbf{A}_I(\phi) \sigma_{IU}), \\ &= (\sigma_{IU}^T \otimes \mathbf{W}^H \mathbf{A}_B(\varphi) \Sigma_{BI}) \text{vec}(\mathbf{A}_I^T(\theta) \bar{\Gamma}_{m_I} \mathbf{A}_I(\phi)), \\ &= (1 \otimes \mathbf{W}^H \mathbf{A}_B(\varphi)) (\sigma_{IU}^T \otimes \Sigma_{BI}) (\mathbf{A}_I^T(\phi) \otimes \mathbf{A}_I^T(\theta)) \text{vec}(\bar{\Gamma}_{m_I}), \\ &= \mathbf{W}^H \mathbf{A}_B(\varphi) (\sigma_{IU}^T \otimes \Sigma_{BI}) (\mathbf{A}_I^T(\phi) \otimes \mathbf{A}_I^T(\theta)) \xi_{m_I}. \end{aligned} \quad (19)$$

Here, we define the *exact equivalent cascaded channel* as

$$\mathbf{G}_{mc} \triangleq \mathbf{A}_B(\varphi) (\sigma_{IU}^T \otimes \Sigma_{BI}) (\mathbf{A}_I^T(\phi) \otimes \mathbf{A}_I^T(\theta)). \quad (20)$$

Based on (19) and (20), we can express the received pilot signal matrix \mathbf{Y} as

$$\mathbf{Y} = \sqrt{P_U} \mathbf{W}^H \mathbf{G}_{mc} \Theta_{mc} + \Omega, \quad (21)$$

where we define $\Theta_{mc} \triangleq [\xi_1, \xi_2, \dots, \xi_{M_I}] \in \mathbb{C}^{N_I^2 \times M_I}$. By applying a vectorization operation, we have

$$\text{vec}(\mathbf{Y} - \Omega) = \sqrt{P_U} (\Theta_{mc}^T \otimes \mathbf{W}^H) \text{vec}(\mathbf{G}_{mc}), \quad (22)$$

$$\begin{aligned} \text{vec}(\mathbf{G}_{mc}) &= \text{vec}(\mathbf{A}_B(\varphi) (\sigma_{IU}^T \otimes \Sigma_{BI}) (\mathbf{A}_I^T(\phi) \otimes \mathbf{A}_I^T(\theta))), \\ &= \underbrace{((\mathbf{A}_I^T(\phi) \otimes \mathbf{A}_I^T(\theta))^T \otimes \mathbf{A}_B(\varphi))}_{\mathbf{D}_{mc}} \text{vec}(\sigma_{IU}^T \otimes \Sigma_{BI}). \end{aligned} \quad (23)$$

By substituting (23) into (22), we obtain

$$\text{vec}(\mathbf{Y} - \Omega) = \sqrt{P_U} \Psi_{mc} \mathbf{D}_{mc} \text{vec}(\sigma_{IU}^T \otimes \Sigma_{BI}), \quad (24)$$

which is the structure of the CS problem. Here, $\Psi_{mc} \triangleq (\Theta_{mc}^T \otimes \mathbf{W}^H) \in \mathbb{C}^{M_B M_I \times N_B N_I^2}$ is the known measurement matrix, and \mathbf{D}_{mc} is the basis matrix. By adopting the CS algorithms, we can recover the equivalent cascaded channel \mathbf{G}_{mc} based on the received signal \mathbf{Y} , since $\text{vec}(\mathbf{G}_{mc}) = \mathbf{D}_{mc} \text{vec}(\sigma_{IU}^T \otimes \Sigma_{BI})$.

Comparing (18) and (24) reveals that accounting for MC results in a dimensional increase in both the measurement and basis matrices. For instance, the dimension of Ψ_{cv} is $M_B M_I \times N_B N_I$, while the dimension of Ψ_{mc} expands to $M_B M_I \times N_B N_I^2$. This enhanced accuracy comes at the expense of *higher complexity*. We will show in Section IV-B that applying the proposed DR strategy can effectively mitigate this complexity issue from an algorithmic perspective.

IV. MC-AWARE RIS CHANNEL ESTIMATION

A. Quantized Dictionaries and CS-Based Channel Estimation

To estimate the equivalent cascaded channel using on-grid CS techniques, we quantize the angular region to a grid of size $G_i = G_i^h G_i^v$, where $i \in \{I, B\}$. Thus, we define the discrete spatial angles as [36]

$$\begin{aligned} \beta_{g_i^h}^h &= \frac{2d_i}{\lambda_c G_i^h} \left(g_i^h - \frac{G_i^h + 1}{2} \right), \quad g_i^h = 1, \dots, G_i^h; G_i^h \geq N_i^h, \\ \beta_{g_i^v}^v &= \frac{2d_i}{\lambda_c G_i^v} \left(g_i^v - \frac{G_i^v + 1}{2} \right), \quad g_i^v = 1, \dots, G_i^v; G_i^v \geq N_i^v. \end{aligned} \quad (25)$$

Accordingly, we obtain the discrete array response matrices $\tilde{\mathbf{A}}_I(\phi) = \tilde{\mathbf{A}}_I(\theta) \in \mathbb{C}^{N_I \times G_I}$ and $\tilde{\mathbf{A}}_B(\varphi) \in \mathbb{C}^{N_B \times G_B}$ as

$$\begin{aligned} [\tilde{\mathbf{A}}_I(\phi)]_{:,g_I^h+(g_I^v-1)G_I^h} &= \frac{1}{\sqrt{N_I}} e^{-j2\pi\beta_{g_I^h}^h \mathbf{n}(N_I^h)} \otimes e^{-j2\pi\beta_{g_I^v}^v \mathbf{n}(N_I^v)}, \\ [\tilde{\mathbf{A}}_B(\varphi)]_{:,g_B^h+(g_B^v-1)G_B^h} &= \frac{1}{\sqrt{N_B}} e^{-j2\pi\beta_{g_B^h}^h \mathbf{n}(N_B^h)} \otimes e^{-j2\pi\beta_{g_B^v}^v \mathbf{n}(N_B^v)}, \end{aligned}$$

According to (17) and (23), we build the conventional and exact dictionary matrices as

$$\tilde{\mathbf{D}}_{cv} = (\tilde{\mathbf{A}}_I^T(\theta) \bullet \tilde{\mathbf{A}}_I^T(\phi))^T \otimes \tilde{\mathbf{A}}_B(\varphi) \in \mathbb{C}^{N_B N_I \times G_B G_I^2}, \quad (26)$$

$$\tilde{\mathbf{D}}_{mc} = (\tilde{\mathbf{A}}_I^T(\phi) \otimes \tilde{\mathbf{A}}_I^T(\theta))^T \otimes \tilde{\mathbf{A}}_B(\varphi) \in \mathbb{C}^{N_B N_I^2 \times G_B G_I^2}. \quad (27)$$

Since redundant columns may be present in $\tilde{\mathbf{D}}_{cv}$ and $\tilde{\mathbf{D}}_{mc}$, we further define $\mathbf{D}_{cv} \in \mathbb{C}^{N_B N_I \times G_{cv}}$ and $\mathbf{D}_{mc} \in \mathbb{C}^{N_B N_I^2 \times G_{mc}}$ as the unique dictionaries that contain only distinct columns. Typically, the conventional structure (26) contains significant redundancy, thus $G_B G_I \leq G_{cv} \ll G_B G_I^2$ [30, Proposition 1]. However, it can be readily verified that $G_{mc} = G_B G_I^2$. This implies that the exact dictionary \mathbf{D}_{mc} not only has a higher dimensionality of atoms but also a greater number of atoms.

By substituting $\tilde{\mathbf{D}}_{cv}/\tilde{\mathbf{D}}_{mc}$ into (18)/(24), we can get the sparse formulation for the conventional/exact model as

$$\mathbf{y} = \text{vec}(\mathbf{Y}) = \sqrt{P_U} \Xi_{\chi} \bar{\sigma}_{\chi} + \text{vec}(\Omega), \quad (28)$$

Algorithm 1 Proposed Two-Stage MC-aware Channel Estimation

- Input:** \mathbf{y} , Ξ_{cv} , Ψ_{mc} , P_U , \hat{L} , and G_{DR} . **Output:** $\hat{\sigma}_{mc}$
- ▷ **Stage 1:** Coarse estimation
- 1: Estimate using OMP $[\hat{\sigma}_{cv}, \Upsilon^{cv}] = \text{OMP}(\mathbf{y}, \Xi_{cv}, P_U, \hat{L})$.
 - ▷ **Stage 2:** Refined estimation
 - 2: Define $\hat{\mathbf{A}}_I = [\hat{\mathbf{A}}_I]_{:, \Upsilon^{cv}}$ according to the indices Υ^{cv} that corresponds to RIS from previous estimated support Υ^{cv} .
 - 3: Construct oversampled dictionaries $\tilde{\mathbf{A}}_{I,S}(\phi)$, $\tilde{\mathbf{A}}_{I,S}(\theta)$ based on (25) with $G_S = g_S G_I$, ($g_S \geq 1$).
 - 4: Define $\hat{\mathbf{A}}_I^S = (\tilde{\mathbf{A}}_{I,S}^T(\phi) \otimes \tilde{\mathbf{A}}_{I,S}^T(\theta))^T$.
 - 5: Apply proposed DR algorithm $\hat{\mathbf{A}}_I^{DR} = \text{DR}(\hat{\mathbf{A}}_I, \hat{\mathbf{A}}_I^S, G_{DR})$.
 - 6: Compute $\Xi_{DR} = \Psi_{mc} \bar{\mathbf{D}}_{DR}$ with $\bar{\mathbf{D}}_{DR} = \hat{\mathbf{A}}_I^{DR} \otimes \hat{\mathbf{A}}_B$.
 - 7: Estimate using OMP $[\hat{\sigma}_{mc}, \Upsilon^{mc}] = \text{OMP}(\mathbf{y}, \Xi_{DR}, P_U, \hat{L})$.
— **DR Algorithm:** $\mathbf{A}_{DR} = \text{DR}(\mathbf{A}, \mathbf{A}_S, \hat{G})$ —
 - 8: Define $\mathbf{A}_T = [\mathbf{A}_S]_{1:N_I, :}$.
 - 9: Compute correlation matrix: $\mathbf{C} = \mathbf{A}_T^H \mathbf{A}$.
 - 10: Select \hat{G} indices from $\sqrt{\text{diag}(\mathbf{C}\mathbf{C}^H)}$ with largest correlation value and populate the index set $\hat{\mathcal{G}}$ with these indices.
 - 11: Return DR matrix $\mathbf{A}_{DR} = [\mathbf{A}_S]_{:, \hat{\mathcal{G}}}$.

where $\Xi_\chi = \Psi_\chi \bar{\mathbf{D}}_\chi \in \mathbb{C}^{M_B M_I \times \bar{G}_\chi}$ is the sensing matrix and $\bar{\sigma}_\chi \in \mathbb{C}^{\bar{G}_\chi}$ is a sparse vector, $\chi \in \{cv, mc\}$. Here, $\bar{\sigma}_\chi$ can be estimated using the CS algorithm such as OMP [47]. Then the equivalent cascaded channel $\mathbf{G}_{cv}/\mathbf{G}_{mc}$ can be recovered based on (17)/(23). Nonetheless, the conventional model-based solution suffers from significant model mismatch due to the neglect of MC, while the exact model-based solution involves a dimensional lift (as seen when comparing the dimensions of the dictionaries $\bar{\mathbf{D}}_{cv}$ and $\bar{\mathbf{D}}_{mc}$). In the following subsection, we propose a two-stage compromise estimation strategy that enjoys the advantages of both methods.

B. Proposed Two-Stage Channel Estimation Strategy

Before presenting our estimation strategy, we elaborate on the motivation behind it. As discussed in Section II-D, the exact model simplifies to the conventional model when $\mathbf{S} = \mathbf{0}$. Although this simplification introduces model mismatch, we can leverage its low complexity to obtain a coarse estimate as prior information for the exact model-based method. This, in turn, helps reduce the complexity of the exact CS solution. Building on this idea, we propose a two-stage estimation algorithm outlined in Algorithm 1. Specifically, the first stage estimates $\bar{\sigma}_{cv}$ by applying OMP to (28) with $\chi = cv$. In the second stage, we utilize the prior information $\hat{\sigma}_{cv}$ and support Υ^{cv} to reduce the search space by shrinking the columns of $(\tilde{\mathbf{A}}_I^T(\phi) \otimes \tilde{\mathbf{A}}_I^T(\theta))^T$ (and consequently $\bar{\mathbf{D}}_{mc}$).⁵

1) *Coarse Estimation:* In the first stage, we apply the OMP algorithm to estimate $\bar{\sigma}_{cv}$ depending on Ξ_{cv} and \hat{L} , as presented in Step 1 of Algorithm 1.⁶ The estimated sparse vector $\hat{\sigma}_{cv}$ is filled based on the detected support Υ^{cv} .

⁵Here, we apply the proposed DR technique to the RIS side only because of the typically larger size of the RIS compared to the BS antenna array. However, the same logic can be applied to the BS.

⁶Details of the OMP algorithm can be found in [47, Algorithm 1]. The parameter \hat{L} is the number of paths to be estimated and assumed different from the actual channel sparsity level because it is unknown.

2) *Refined Estimation:* In the second stage, we perform exact CS estimation with prior information of a coarse estimate.⁷ For illustrative convenience, we define $\check{\mathbf{A}}_I \triangleq (\hat{\mathbf{A}}_I^T(\theta) \otimes \tilde{\mathbf{A}}_I^T(\phi))^T \in \mathbb{C}^{N_I \times G_I^2}$. In step 2 of Algorithm 1, we construct $\hat{\mathbf{A}}_I \in \mathbb{C}^{N_I \times \hat{L}}$, a matrix consisting of the columns of $\check{\mathbf{A}}_I$ corresponding to the support Υ^{cv} obtained in step 1. This dictionary represents the spatial angles to limit the search space over and is the first input for the proposed DR algorithm. The second input is the oversampled dictionary $\hat{\mathbf{A}}_I^S$ defined in steps 3 and 4 of Algorithm 1. We apply the proposed DR algorithm in step 5, where the idea is to extract only a small number of columns from the $\hat{\mathbf{A}}_I^S$ that has the same form of $(\hat{\mathbf{A}}_I^T \otimes \hat{\mathbf{A}}_I^T)^T$ and used to get $\bar{\mathbf{D}}_{mc}$ (steps 8-11). The selected G_{DR} columns have the highest correlation with $\hat{\mathbf{A}}_I$ (from step 2) and correspond to the most probable spatial angles where the channel is expected to be. We define $G_{DR} = \rho_{DR} \bar{G}_{cv} / G_B \ll G_I^2$ ($0 < \rho_{DR} \leq 1$) for the proposed approach to be less complex yet accurate. In step 6, by using $\hat{\mathbf{A}}_I^{DR}$ of step 5, we compute the DR sensing matrix to be later used in step 7 where we apply the OMP algorithm. The output $\hat{\sigma}_{mc}$ is an estimate of $\bar{\sigma}_{mc}$ defined in (28). Finally, the exact equivalent cascaded channel \mathbf{G}_{mc} can be recovered as $\text{vec}(\hat{\mathbf{G}}_{mc}) = \bar{\mathbf{D}}_{DR} \hat{\sigma}_{mc}$.

V. MUTUAL COUPLING-AWARE JOINT BEAMFORMING**A. Problem Formulation**

Suppose an equivalent channel \mathbf{G}_{mc} is available. Based on (19) and (20), the joint beamforming task refers to solving the following optimization problem:

$$\begin{aligned} \max_{\mathbf{w}, \gamma} \quad & |\mathbf{w}^H \mathbf{G}_{mc} \text{vec}((\text{diag}(\gamma)^{-1} - \mathbf{S})^{-1})|, \\ \text{s.t.} \quad & \|\mathbf{w}\|_2^2 \leq P_B, \quad \|\gamma\|_2^2 \leq P_I. \end{aligned} \quad (29)$$

As an initial work on the RIS mutual coupling-aware beamforming, here we simply consider a fully digital combiner with a power constraint $\|\mathbf{w}\|_2^2 \leq P_B$. Such a constraint for beamforming has been widely adopted in the literature, see e.g. [49], [52]. The same power constraint is also applied to the active RIS configuration, i.e., $\|\gamma\|_2^2 \leq P_I$.

Because (29) is a joint optimization problem over \mathbf{w} and γ , we adopt an alternating optimization strategy to solve it [53]. Specifically, we iterate over the steps of (i) optimizing \mathbf{w} given a fixed γ and then (ii) optimizing γ given the updated \mathbf{w} . The following subsections will formulate and analyze the two individual subproblems.

B. BS Combining: A Simple Closed-Form Solution

Given a feasible γ and defining $\mathbf{r} \triangleq \mathbf{G}_{mc} \text{vec}((\text{diag}(\gamma)^{-1} - \mathbf{S})^{-1})$, the joint problem (29) is reduced into

$$\max_{\mathbf{w}} |\mathbf{w}^H \mathbf{r}|, \quad \text{s.t.} \quad \|\mathbf{w}\|_2^2 \leq P_B. \quad (30)$$

Here, we can rewrite the objective function as $|\mathbf{w}^H \mathbf{r}|^2 = \mathbf{w}^H \mathbf{r} \mathbf{r}^H \mathbf{w}$ without changing the optimal solution. Hence, the solution to problem (30) is given by

$$\mathbf{w}_* = \sqrt{P_B} \mathbf{u}_{\max}(\mathbf{r} \mathbf{r}^H), \quad (31)$$

⁷This prior information can be obtained either through the conventional model-based CS estimation described in Section IV-B1 or from the previous exact CS estimation.

where $\mathbf{u}_{\max}(\mathbf{M})$ denotes the eigenvector corresponding to the largest eigenvalue of a square matrix \mathbf{M} . This solution can be directly obtained based on the inequality $\mathbf{x}^H \mathbf{M} \mathbf{x} \leq \lambda_{\max}(\mathbf{M}) \mathbf{x}^H \mathbf{x}$, given \mathbf{M} is a Hermitian matrix [54], [55]. Here, $\lambda_{\max}(\mathbf{M})$ denotes the largest eigenvalue of \mathbf{M} and the equality holds when $\mathbf{x} = k \mathbf{u}_{\max}(\mathbf{M})$, $\forall k \in \mathbb{R}$. Therefore, we have $\mathbf{w}^H \mathbf{r} \mathbf{r}^H \mathbf{w} \leq \lambda_{\max}(\mathbf{r} \mathbf{r}^H) \mathbf{w}^H \mathbf{w} \leq \lambda_{\max}(\mathbf{r} \mathbf{r}^H) P_B$. It can be easily checked that the two equalities hold with solution (31).

C. RIS Beamforming: Approximation and Reformulation

Given a feasible \mathbf{w} and defining $\mathbf{t} \triangleq \mathbf{G}_{\text{mc}}^H \mathbf{w}$, the joint problem (29) is reduced into

$$\begin{aligned} \max_{\gamma} \quad & |\mathbf{t}^H \text{vec}((\text{diag}(\gamma)^{-1} - \mathbf{S})^{-1})|, \\ \text{s.t.} \quad & \|\gamma\|_2^2 \leq P_1. \end{aligned} \quad (32)$$

The matrix inversion in the objective function poses significant challenges for optimization. To circumvent this intractable process, we leverage the Neumann series expansion [56]

$$(\mathbf{\Gamma}^{-1} - \mathbf{S})^{-1} = \left(\sum_{n=0}^{\infty} (\mathbf{\Gamma} \mathbf{S})^n \right) \mathbf{\Gamma} = \mathbf{\Gamma} + \mathbf{\Gamma} \mathbf{S} \mathbf{\Gamma} + \mathbf{\Gamma} \mathbf{S} \mathbf{\Gamma} \mathbf{S} \mathbf{\Gamma} + \dots \quad (33)$$

This series expansion has been widely utilized in the analysis of the mutual coupling in array signal processing [28], [45], [46]. Note that this expansion holds only when all the eigenvalues of $\mathbf{\Gamma} \mathbf{S}$ are within the unit circle, i.e., $|\lambda_i(\mathbf{\Gamma} \mathbf{S})| < 1$, $\forall i = 1, \dots, N_L$. Fortunately, such a condition can be satisfied and the expression is valid for a typical MC strength.

Remark 2: When only the first term is considered, (33) reduces to the conventional model without RIS MC.

By retaining the first two terms of (33), $(\mathbf{\Gamma}^{-1} - \mathbf{S})^{-1} \approx \mathbf{\Gamma} + \mathbf{\Gamma} \mathbf{S} \mathbf{\Gamma}$, and we can rewrite (32) as

$$\begin{aligned} \min_{\gamma} \quad & -|\mathbf{t}^H \text{vec}(\text{diag}(\gamma) + \text{diag}(\gamma) \mathbf{S} \text{diag}(\gamma))|^2, \\ \text{s.t.} \quad & \|\gamma\|_2^2 \leq P_1. \end{aligned} \quad (34)$$

Notice the following relationship:

$$\mathbf{t}^H \text{vec}(\text{diag}(\gamma)) = (\text{diag}^{-1}(\text{vec}^{-1}(\mathbf{t})))^H \gamma, \quad (35)$$

$$\mathbf{t}^H \text{vec}(\text{diag}(\gamma) \mathbf{S} \text{diag}(\gamma)) = \gamma^T (\mathbf{S} \odot (\text{vec}^{-1}(\mathbf{t}))^*) \gamma. \quad (36)$$

Defining $\mathbf{q} \triangleq \text{diag}^{-1}(\text{vec}^{-1}(\mathbf{t}))$, $\mathbf{B} \triangleq \mathbf{S} \odot (\text{vec}^{-1}(\mathbf{t}))^*$, we can rewrite (34) as

$$\begin{aligned} \min_{\gamma} \quad & -(\mathbf{q}^H \gamma + \gamma^T \mathbf{B} \gamma)^H (\mathbf{q}^H \gamma + \gamma^T \mathbf{B} \gamma), \\ \text{s.t.} \quad & \|\gamma\|_2^2 \leq P_1. \end{aligned} \quad (37)$$

Although simplified, problem (37) is still challenging due to its non-convexity. In Section VI, we will adopt the SCA framework to solve this problem.

VI. RIS CONFIGURATION OPTIMIZATION VIA SCA

This section presents an iterative solution to the non-convex optimization problem (37) by utilizing the SCA framework. We first briefly review the fundamentals of SCA and then demonstrate how to apply this framework to solve (37).

A. Background of Successive Convex Approximation

SCA is a general framework that can decompose a complex optimization problem into a series of simpler optimization problems [57], [58]. Consider the following general optimization problem as an example:

$$\min_{\mathbf{x}} f(\mathbf{x}), \quad \text{s.t. } \mathbf{x} \in \mathcal{X}. \quad (38)$$

The SCA framework generates a sequence of descending feasible points $\{\mathbf{x}_i\}_{i \in \mathbb{N}}$ through a cyclic application of two steps: (i) formulating a simpler surrogate function (which is convex) at the current feasible point, and (ii) optimizing the surrogate function to acquire an improved feasible point.

1) *Formulating Surrogate Functions:* At each feasible point \mathbf{x}_i , the SCA method formulates a surrogate function $g(\mathbf{x}|\mathbf{x}_i)$ satisfying the following two conditions:

Condition 1: $g(\mathbf{x}|\mathbf{x}_i)$ is convex on \mathcal{X} , $\forall \mathbf{x}_i \in \mathcal{X}$.

Condition 2: $g(\mathbf{x}|\mathbf{x}_i)$ is differentiable on \mathcal{X} and its gradient equals to the gradient of $f(\mathbf{x})$ at \mathbf{x}_i , i.e., $\nabla g(\mathbf{x}|\mathbf{x}_i)|_{\mathbf{x}=\mathbf{x}_i} = \nabla f(\mathbf{x})|_{\mathbf{x}=\mathbf{x}_i}$.

2) *Optimizing Surrogate Functions:* Once a surrogate function $g(\mathbf{x}|\mathbf{x}_i)$ that satisfies Condition 1 and Condition 2 is obtained, we can obtain a descending direction of $f(\mathbf{x})$ by addressing the following convex optimization problem:

$$\hat{\mathbf{x}}_{i+1} = \arg \min_{\mathbf{x}} g(\mathbf{x}|\mathbf{x}_i), \quad \text{s.t. } \mathbf{x} \in \mathcal{X}. \quad (39)$$

Then, we update the feasible point as $\mathbf{x}_{i+1} = \mathbf{x}_i + \eta_i (\hat{\mathbf{x}}_{i+1} - \mathbf{x}_i)$, where $\eta_i \in \mathbb{R}^+$ is the step size. Various rules for selecting the step size are outlined in [58, Assumption 3.6], and the convergence of this iterative SCA procedure has been established by [58, Theorem 3.7].

B. Successive Convex Approximation of (37)

Based on the SCA principle presented in Section VI-A, the following Proposition 1 proposes a surrogate function for the objective function in (37).

Proposition 1: For an arbitrary feasible point γ_i to (37), an associated surrogate function that satisfies Condition 1 and Condition 2 can be formulated as

$$\begin{aligned} g(\gamma|\gamma_i) = & -\gamma^H \mathbf{q} \mathbf{q}^H \gamma - \gamma^H \mathbf{q} \gamma_i^T \mathbf{B} \gamma - \gamma^H \mathbf{B}^H \gamma_i^* \mathbf{q}^H \gamma \\ & - \gamma^H \mathbf{B}^H \gamma_i^* \gamma_i^T \mathbf{B} \gamma + K \|\gamma - \gamma_i\|_2^2 - \gamma_i^H \mathbf{q} \gamma^T \mathbf{B} \gamma_i \\ & - \gamma_i^H \mathbf{B}^H \gamma^* \mathbf{q}^H \gamma_i - \gamma_i^H \mathbf{B}^H \gamma^* \gamma_i^T \mathbf{B} \gamma_i - \gamma_i^H \mathbf{B}^H \gamma_i^* \gamma^T \mathbf{B} \gamma_i. \end{aligned} \quad (40)$$

Here, $K \in \mathbb{R}^+$ is a parameter that must be chosen to ensure

$$K \geq \lambda_{\max}(\mathbf{Q}_i), \quad (41)$$

where

$$\mathbf{Q}_i = \mathbf{q} \mathbf{q}^H + \mathbf{q} \gamma_i^T \mathbf{B} + \mathbf{B}^H \gamma_i^* \mathbf{q}^H + \mathbf{B}^H \gamma_i^* \gamma_i^T \mathbf{B}. \quad (42)$$

Because \mathbf{Q}_i is a hermitian matrix, all its eigenvalues are real, resulting in a real K in (41).

Proof: See Appendix A. \square

C. Solving the Surrogate Optimization Problem

For the second step of SCA, we now consider optimizing the surrogate function $g(\gamma|\gamma_i)$. Based on (40), this surrogate optimization problem can be formulated as

$$\begin{aligned} \min_{\gamma} \quad & \gamma^H(K\mathbf{I} - \mathbf{Q}_i)\gamma - \mathbf{b}_i^T\gamma - \mathbf{b}_i^H\gamma^*, \\ \text{s.t.} \quad & \|\gamma\|_2^2 \leq P_1, \end{aligned} \quad (43)$$

where $\mathbf{b}_i = K\gamma_i^* + (\gamma_i^H\mathbf{q} + \gamma_i^H\mathbf{B}^H\gamma_i^*)\mathbf{B}\gamma_i$. Note that we omit the constant term in the objective function of (43).

Since the objective function $g(\gamma|\gamma_i)$ and the inequality constraint $\|\gamma\|_2^2 - P_1$ in (43) are convex, and there exists strictly feasible points satisfying $\|\gamma\|_2^2 < P_1$, the Slater's condition is satisfied [54, Sec. 5.2.3]. Therefore, the strong duality holds for (43) and the optimal solution of (43) can be found based on the Karush-Kuhn-Tucker (KKT) conditions.

To begin with, the Lagrangian associated with the problem (43) is derived as

$$L(\gamma, \nu) = \gamma^H(K\mathbf{I} - \mathbf{Q}_i)\gamma - \mathbf{b}_i^T\gamma - \mathbf{b}_i^H\gamma^* + \nu(\gamma^H\gamma - P_1), \quad (44)$$

where $\nu \in \mathbb{R}_{\geq 0}$ is the Lagrange multiplier (or dual variable) associated with the inequality constraint. Then, the KKT conditions indicate that the optimal primal and dual points, denoted as (γ_o, ν_o) , must satisfy the following conditions:

$$\nabla_{\gamma}L(\gamma_o, \nu_o) = \mathbf{0}, \quad (45)$$

$$\nu_o(\gamma_o^H\gamma_o - P_1) = 0, \quad (46)$$

$$\nu_o \geq 0, \quad (47)$$

$$(\gamma_o^H\gamma_o - P_1) \leq 0. \quad (48)$$

Based on (45), we have

$$\frac{\partial L(\gamma_o, \nu_o)}{\partial \gamma_o^*} = \left(\frac{\partial L(\gamma_o, \nu_o)}{\partial \gamma_o} \right)^* = (K\mathbf{I} - \mathbf{Q}_i)\gamma_o - \mathbf{b}_i^* + \nu_o\gamma_o = \mathbf{0}.$$

This immediately yields $\gamma_o = ((K + \nu_o)\mathbf{I} - \mathbf{Q}_i)^{-1}\mathbf{b}_i^*$. The conditions in (41) and (47) guarantee that all eigenvalues of $((K + \nu_o)\mathbf{I} - \mathbf{Q}_i)$ lie in $\mathbb{R}_{\geq 0}$; thus, this matrix is always invertible. Subsequently, the value of the optimal primal solution γ_o can be inferred in the following two cases:

1) $\nu_o = 0$: In this case, the optimal primal solution is

$$\gamma_o = \begin{cases} (K\mathbf{I} - \mathbf{Q}_i)^{-1}\mathbf{b}_i^*, & \text{if } |(K\mathbf{I} - \mathbf{Q}_i)^{-1}\mathbf{b}_i^*|^2 \leq P_1, \\ \text{does not exist,} & \text{otherwise.} \end{cases} \quad (49)$$

2) $\nu_o > 0$: In this case, the optimal primal solution γ_o must satisfy

$$\begin{cases} \gamma_o = ((K + \nu_o)\mathbf{I} - \mathbf{Q}_i)^{-1}\mathbf{b}_i^*, & (50) \\ |\gamma_o|^2 = P_1. & (51) \end{cases}$$

By observing (50), we see that $|\gamma_o|^2$ is monotonically decreasing w.r.t ν_o . Therefore, we can infer

$$\gamma_o = \begin{cases} \text{does not exist,} & \text{if } |(K\mathbf{I} - \mathbf{Q}_i)^{-1}\mathbf{b}_i^*|^2 \leq P_1, \\ \text{solution of (50) and (51),} & \text{otherwise.} \end{cases}$$

Here, equations (50) and (51) can be solved by performing an expansion-and-shrink search on ν_o . Algorithm 2 summarizes the steps of solving the surrogate problem (43).

Algorithm 2 Expansion-and-Shrink Search Solution to (43)

```

1: Input:  $\mathbf{Q}_i, \mathbf{b}_i, P_1, K$ .   Output:  $\gamma_o$ .
2: if  $|((K\mathbf{I} - \mathbf{Q}_i)^{-1}\mathbf{b}_i^*)|^2 \leq P_1$  then
3:    $\gamma_o = (K\mathbf{I} - \mathbf{Q}_i)^{-1}\mathbf{b}_i^*$ .
4: else
5:   Initialize  $\ell = 1, u = \ell + 1, \varsigma = 1 \times 10^{-3}$ .
6:   Set expansion-and-shrink rate  $\varepsilon_\ell \in (0, 1)$  and  $\varepsilon_u > 1$ .
7:   while  $u - \ell > \varsigma$  do
8:     Compute  $P_\ell = |((K + \ell)\mathbf{I} - \mathbf{Q}_i)^{-1}\mathbf{b}_i^*|^2$ .
9:     Compute  $P_u = |((K + u)\mathbf{I} - \mathbf{Q}_i)^{-1}\mathbf{b}_i^*|^2$ .
10:    if  $P_\ell < P_1$  and  $P_u < P_1$  then
11:       $u = \ell, \ell = \varepsilon_\ell \ell$ .
12:    else if  $P_\ell > P_1$  and  $P_u > P_1$  then
13:       $\ell = u, u = \varepsilon_u u$ .
14:    else
15:      Compute  $P_m = |((K + \frac{\ell+u}{2})\mathbf{I} - \mathbf{Q}_i)^{-1}\mathbf{b}_i^*|^2$ .
16:      if  $P_m \leq P_1$  then
17:         $u = (\ell + u)/2$ .
18:      else
19:         $\ell = (\ell + u)/2$ .
20:    $\gamma_o = ((K + \frac{\ell+u}{2})\mathbf{I} - \mathbf{Q}_i)^{-1}\mathbf{b}_i^*$ .

```

Algorithm 3 Solving (37) Using SCA

```

1: Input:  $\mathbf{q}, \mathbf{B}, P_1$ .   Output:  $\gamma_*$ .
2: Initialize  $i = 0$  and randomly select  $\gamma_0, \|\gamma_0\|^2 \leq P_1$ .
3: for  $i \in \mathbb{N}$  do
4:   Compute  $\mathbf{Q}_i$  using (42) and select  $K \geq \lambda_{\max}(\mathbf{Q}_i)$ .
5:   Compute  $\mathbf{b}_i = K\gamma_i^* + (\gamma_i^H\mathbf{q} + \gamma_i^H\mathbf{B}^H\gamma_i^*)\mathbf{B}\gamma_i$ .
6:   Apply Algorithm 2 to solve (43) and obtain  $\gamma_o$ .
7:   Let  $\tilde{\gamma}_{i+1} = \gamma_o$  and choose a step size  $\eta_i$  through (52).
8:   Update  $\gamma_{i+1} = \gamma_i + \eta_i(\tilde{\gamma}_{i+1} - \gamma_i)$ .
9:   Stop if  $\|\gamma_{i+1} - \gamma_i\|$  is lower than a preset threshold.
return  $\gamma_* = \gamma_{i+1}$ .

```

D. Solving (37) Using SCA

Based on the convex approximation in Section VI-B and the corresponding solution in Section VI-C, we summarize the complete SCA procedure for solving (37) in Algorithm 3, which follows the SCA principle in Section VI-A. As mentioned, the step size η_i of the iteration can be chosen according to different rules. As an example, here we present a line search rule [58] for determining η_i . Let $f(\gamma)$ denote the objective function in (37) and choose $\delta_1, \delta_2 \in (0, 1)$. The line search rule chooses $\eta_i = \delta_1^{n_i}$, where n_i is the smallest natural number satisfying

$$f(\gamma_i + \eta_i\Delta\gamma_i) \leq f(\gamma_i) + \delta_2\eta_i\left((\nabla_{\gamma^*}f(\gamma_i))^H\Delta\gamma_i\right), \quad (52)$$

where $\Delta\gamma_i \triangleq \tilde{\gamma}_{i+1} - \gamma_i$ and $\tilde{\gamma}_{i+1}$ denotes the solution of (43). Here, $\nabla_{\gamma^*}f(\gamma_i) = \partial f(\gamma_i)/\partial \gamma^*$, which is the direction where f increases fastest at γ_i [59, Theorem 3.4].

VII. SIMULATION RESULTS AND DISCUSSION

A. Simulation Setup

Throughout the simulations, we position the UE at $2.6 \text{ m} \times [\sin \frac{\pi}{6}, \cos \frac{\pi}{6}, 0]^T$, the RIS at $[0, 0, 0]^T$ facing the positive

Y-axis, and the BS at $2.2 \text{ m} \times [\sin \frac{\pi}{3}, \cos \frac{\pi}{3}, 0]^\top$ facing the negative Y-axis, consistent with the far-field measurement setup in [48]. We set the signal frequency $f_c = 30 \text{ GHz}$ and the thermal noise power $\sigma_B^2 = \sigma_I^2 = -95 \text{ dBm}$, according to [48, Fig. 25]. The RIS is composed of $N_I = 8 \times 2$ elements with $d_I = \lambda_c/20$ while the BS deploys $N_B = 3 \times 3$ elements with $d_B = \lambda_c/2$. Regarding the channel generation, we use $L_U = 4$, the LoS path gain in (1) is $\alpha_1 = (\lambda_c/(4\pi d_{IU}))^{\gamma_{IU}/2}$, where d_{IU} is the distance between the UE and RIS, and the path loss exponent $\gamma_{IU} = 2.1$. For NLoS paths $\alpha_\ell \sim \mathcal{CN}(0, \alpha_1^2)$. The same logic applies to ρ_ℓ in (4) with $L_B = 2$.

The scattering matrix \mathbf{S} is obtained by first calculating the mutual impedances (\mathbf{Z} matrix) based on the analytical model in [18, Eq.(2)]. Then, it is converted to scattering parameters (\mathbf{S} matrix) by applying $\mathbf{S} = (\mathbf{Z} + Z_0\mathbf{I})^{-1}(\mathbf{Z} - Z_0\mathbf{I})$ [26, Eq.(24)], where $Z_0 = 50 \Omega$ is the characteristic impedance. Here, \mathbf{S} is a function of RIS inter-element spacing, with denser element integration typically resulting in stronger mutual coupling [18, Fig. 2]. Unless stated otherwise, we set $P_I = 400$, i.e., the RIS has an average amplification factor $\bar{a} = \sqrt{P_I/N_I} = 5$. The training uses random phase shifts, uniformly distributed as $\mathcal{U}(0, 2\pi)$. We perform 40 trials to average results. We set $\hat{L} = 20$, $G_I = N_I$, $G_B = N_B$, and $g_S = 1$.

B. Performance Metrics

Based on Section III and Section IV, we can estimate the conventional and exact equivalent cascaded channel $\hat{\mathbf{G}}_{cv} \in \mathbb{C}^{N_B \times N_I}$ and $\hat{\mathbf{G}}_{mc} \in \mathbb{C}^{N_B \times N_I^2}$ based on the conventional MC-unaware model and the exact MC-aware model, respectively. Since $\hat{\mathbf{G}}_{cv}$ and $\hat{\mathbf{G}}_{mc}$ have different dimensions, for a fair comparison, we evaluate the estimation accuracy by computing the normalized mean squared error (NMSE) of the reconstructed received signal as

$$\text{NMSE}_{cv} = \mathbb{E} \|\sqrt{P_U} \mathbf{W}^H \hat{\mathbf{G}}_{cv} \boldsymbol{\Theta}_{cv} - \bar{\mathbf{Y}}\|_{\mathbb{F}}^2 / \|\bar{\mathbf{Y}}\|_{\mathbb{F}}^2, \quad (53)$$

$$\text{NMSE}_{mc} = \mathbb{E} \|\sqrt{P_U} \mathbf{W}^H \hat{\mathbf{G}}_{mc} \boldsymbol{\Theta}_{mc} - \bar{\mathbf{Y}}\|_{\mathbb{F}}^2 / \|\bar{\mathbf{Y}}\|_{\mathbb{F}}^2, \quad (54)$$

where $\bar{\mathbf{Y}}$ is the noise-free version of the received signal.

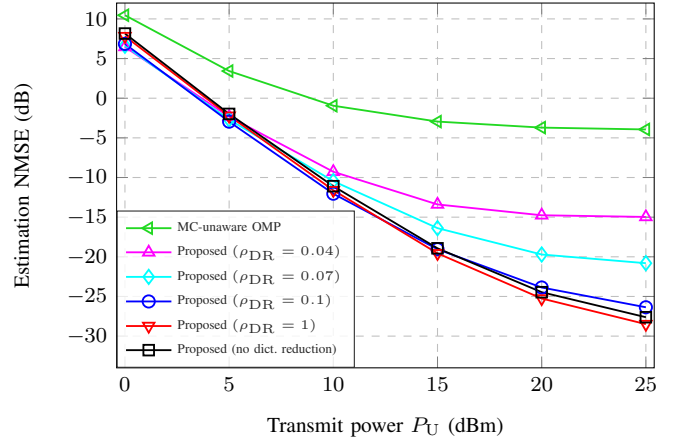
The computational complexity of Algorithm 1 is dominated by OMP's complexity that mainly depends on the used sensing matrix $\boldsymbol{\Xi}$ size, $\mathcal{C}_{\text{OMP}} = \mathcal{O}(\hat{L}M_I M_B J(\boldsymbol{\Xi}))$ [37]. Here, $J(\boldsymbol{\Xi})$ denotes the number of columns of the used $\boldsymbol{\Xi}$. Hence, we define the effective size metric $\zeta_\nu = J(\boldsymbol{\Xi}_\nu)/J(\boldsymbol{\Xi}_{mc})$, $\nu \in \{cv, DR\}$ as the ratio of sensing matrix columns for the adopted method to the exact model sensing matrix columns.

For the beamforming performance, we evaluate the spectral efficiency of given $\{\mathbf{w}, \boldsymbol{\gamma}\}$ as

$$\text{SE} = \log_2 \left(1 + \frac{P_T |\mathbf{w}^H \mathbf{H}_{BI} (\text{diag}(\boldsymbol{\gamma})^{-1} - \mathbf{S})^{-1} \mathbf{h}_{IU}|^2}{P_B \sigma_B^2 + \|\mathbf{w}^H \mathbf{H}_{BI} (\text{diag}(\boldsymbol{\gamma})^{-1} - \mathbf{S})^{-1}\|_2^2 \sigma_I^2} \right). \quad (55)$$

C. Channel Estimation Performance Evaluation

Fig. 3(a) presents the channel estimation NMSE versus transmit power. As demonstrated, the proposed two-stage algorithm consistently outperforms the conventional MC-unaware OMP in the presence of MC. Even for small values of ρ_{DR} , our method achieves several dB improvements in accuracy compared to the conventional approach. Furthermore, the



(a) Channel estimation NMSE versus transmit power

| Method | Conv. | $\rho_{DR} = 0.04$ | $\rho_{DR} = 0.07$ | $\rho_{DR} = 0.1$ | $\rho_{DR} = 1$ |
|-------------|--------|--------------------|--------------------|-------------------|-----------------|
| ζ_ν | 53.13% | 1.95% | 3.91% | 5.47% | 53.13% |

(b) Effective size for different methods

Fig. 3. Performance evaluation of channel estimation: (a) Accuracy assessed by NMSE. (b) Computational complexity assessed by effective size.

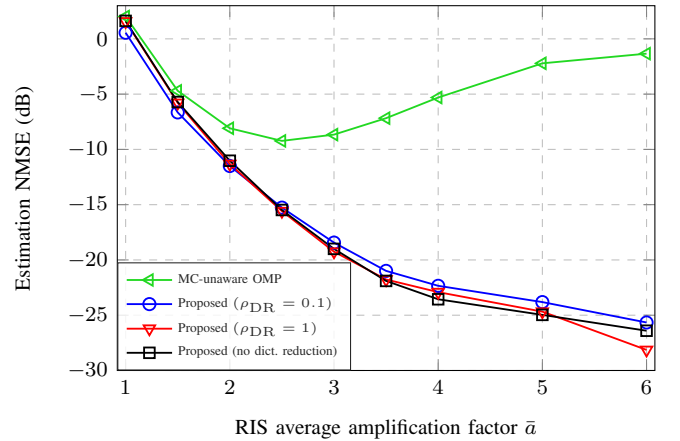


Fig. 4. Evaluation of the channel estimation NMSE versus RIS average amplification factor $\bar{a} = \sqrt{P_I/N_I}$. As highlighted in Remark 1, higher amplification intensifies the impact of MC.

accuracy of the estimation increases with greater ρ_{DR} . For $\rho_{DR} \geq 0.1$, the proposed algorithm performs on par with the direct MC-aware OMP (without dictionary reduction). However, as depicted in Fig. 3(b), lower ρ_{DR} results in reduced complexity, highlighting a trade-off between performance and complexity. Notably, when $\rho_{DR} = 0.1$, the dictionary size of our method is only 5.47% of that in the direct MC-aware OMP, while still achieving comparable performance, demonstrating the superiority of the proposed approach.

Fig. 4 examines the effect of the RIS amplification factor on channel estimation accuracy. We observe that under a low amplification factor ($\bar{a} \leq 1.5$), the conventional and proposed methods perform similarly, both with accuracy improving as the RIS amplification increases, indicating a negligible impact of MC. However, as the RIS amplification factor continues to increase, the performance of the conventional MC-unaware OMP deteriorates and diverges from the proposed method due to the stronger impact of MC, as analyzed in Remark 1. Notably, when $\bar{a} > 2.5$, channel estimation performance even

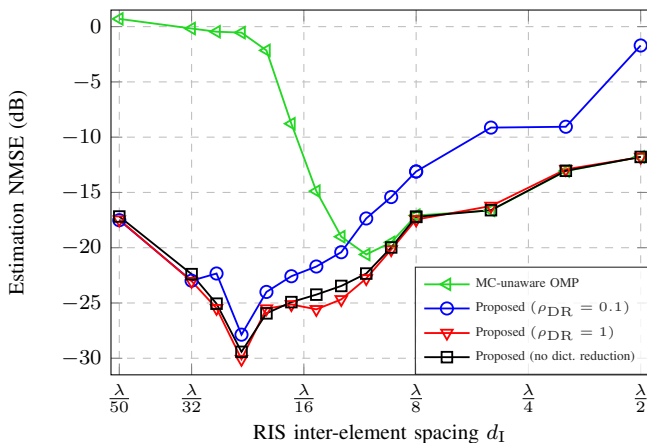


Fig. 5. Evaluation of the channel estimation NMSE versus RIS inter-element spacing. A shorter spacing typically causes stronger MC effect [18, Fig. 2].

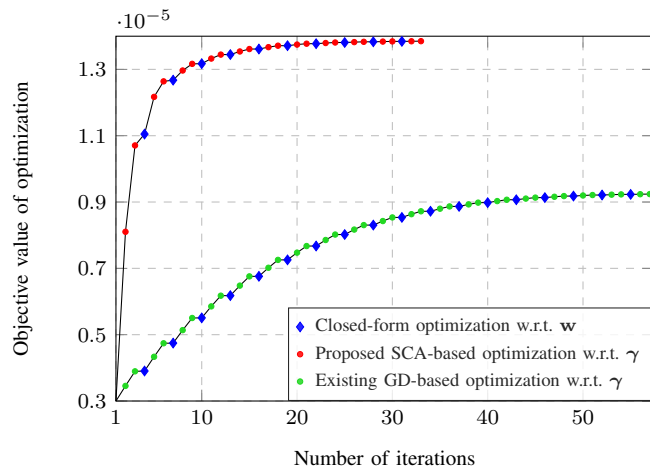


Fig. 6. Comparison of the proposed SCA and existing GD methods by presenting the beamforming optimization objective value against the number of iterations.

degrades with further increases in RIS amplification. This suggests that simply increasing RIS power is not always beneficial unless MC is well managed. In contrast, our proposed method effectively accounts for the MC mechanism, allowing it to consistently benefit from increased RIS amplification, even with a low dictionary reduction factor, such as $\rho_{DR} = 0.1$.

In Fig. 5, the effect of different MC levels is investigated by varying the RIS inter-element spacing. When the RIS spacing is large ($d_I > \lambda/8$), the MC effect is weak, and thus the performance of the MC-unaware OMP and the proposed method with appropriate dictionary reduction factors ($\rho_{DR} \geq 1$ or no reduction) is similar. Nevertheless, with shorter RIS spacing ($d_I < \lambda/8$), the MC-unaware OMP suffers significant performance degradation, which is exacerbated as the MC effect intensifies. The proposed method, however, maintains a performance gain of over 15 dB under strong-MC conditions. An additional observation is that careful selection of the dictionary reduction factor ρ_{DR} is essential, especially in scenarios with minimal MC (e.g., $d_I > \lambda/8$).

D. Beamforming Performance Evaluation

Fig. 6 depicts the beamforming optimization objective value in (29) over the iteration of our proposed SCA and the existing

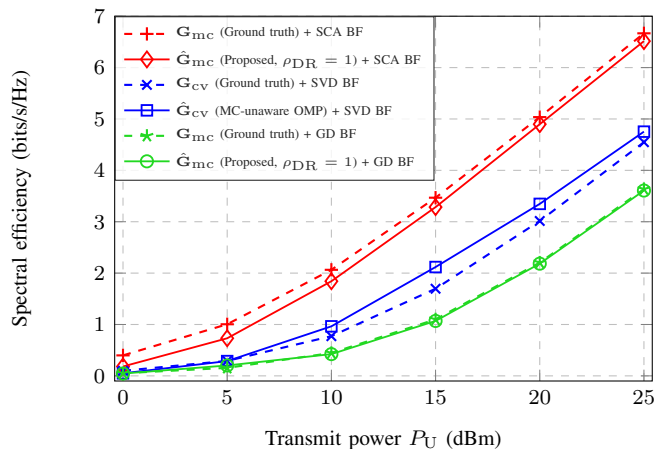


Fig. 7. Performance evaluation of spectral efficiency versus transmit power for different estimation and beamforming methods.

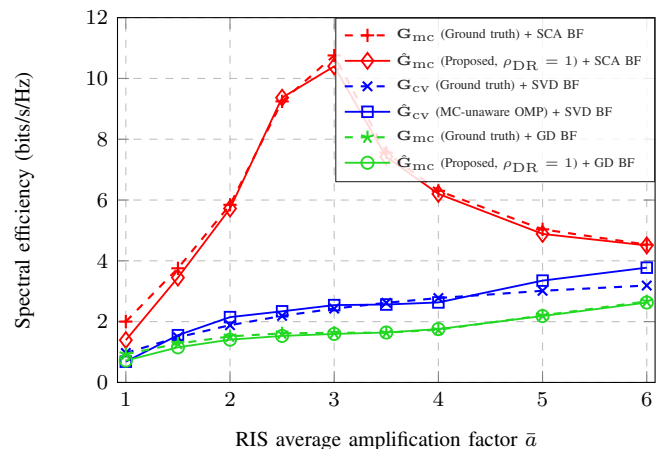


Fig. 8. Evaluation of spectral efficiency versus RIS average amplification factor $\bar{a} = \sqrt{P_I/N_I}$. As highlighted in Remark 1, higher amplification intensifies the impact of MC.

GD algorithm, given the ground truth cascaded channel \mathbf{G}_{mc} . The proposed SCA secures two gains compared to GD: (i) higher beamforming gain, and (ii) higher efficiency (less number of iterations). For example, with 20 iterations, SCA achieves almost twice the gain compared to GD.

Fig. 7 evaluates the spectral efficiency of different channel estimation and beamforming methods by changing the transmit power P_U . In addition to the MC-aware beamforming approaches based on \mathbf{G}_{mc} (using either SCA or GD), we also assess the conventional MC-unaware beamforming based on \mathbf{G}_{cv} , which is addressed using singular value decomposition (SVD) [60]. It is evident that the proposed SCA-based MC-aware beamforming solution achieves the highest spectral efficiency. Moreover, the spectral efficiency achieved with the estimated $\hat{\mathbf{G}}_{mc}$ from the proposed channel estimation method is only slightly lower than that achieved with the ground truth channel, which again confirms the effectiveness of the proposed channel estimator. A similar trend is observed with the GD-based MC-aware beamforming method. However, in the SVD-based MC-unaware beamforming, the ground truth channel does not always result in the highest spectral efficiency due to model mismatch from neglecting MC. Despite this, the SVD-based approach still outperforms the GD-based MC-

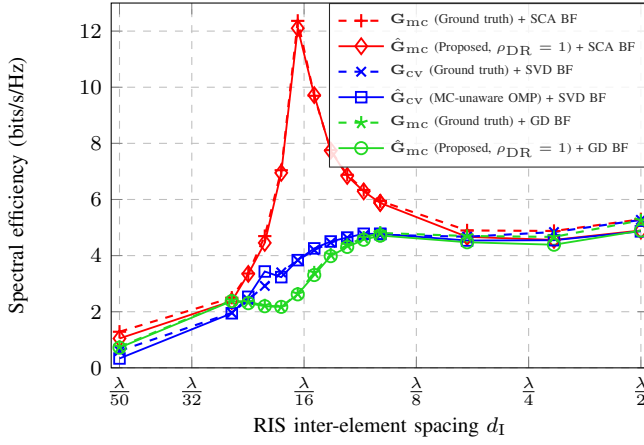


Fig. 9. Evaluation of the spectral efficiency versus RIS inter-element spacing. A shorter spacing typically causes stronger MC effect [18, Fig. 2].

aware beamforming. This indicates that appropriately addressing nonlinearity issues is crucial for leveraging MC-awareness to enhance communication performance, underscoring the importance of the proposed SCA-based beamforming algorithm.

Analogous to Fig. 4 and Fig. 5, Fig. 8 and Fig. 9 assess the spectral efficiency with varying RIS amplification factors and inter-element spacings, respectively. Both figures demonstrate that the proposed SCA-based MC-aware beamforming method consistently achieves the highest spectral efficiency. An interesting observation is that, as the impact of MC increases, the performance gain of the proposed SCA-based solution initially improves but eventually declines. This occurs because the Neumann series approximation (33) becomes less accurate when MC is excessively strong. In addition, in Fig. 9, we note a significant high spectral efficiency around $d_I = \lambda/16$. Since this setup does not increase RIS power but only shifts the inter-element spacing, it suggests that with sophisticated signal processing solutions, additional gains can be obtained from MC. This observation indicates that the prevailing view of MC as solely a negative effect is biased.

VIII. CONCLUSION

This paper addresses the challenges of channel estimation and beamforming in active RIS-assisted communication systems in the presence of MC. Our findings demonstrate that conventional MC-unaware channel estimators underperform in scenarios with strong MC, highlighting the need for accurate modeling and novel algorithms. By employing the CS and DR techniques, we propose a low-complexity yet accurate channel estimator that performs effectively under strong MC conditions. Moreover, we reveal that even with accurate channel estimation, an effective MC-aware beamforming approach is essential for achieving decent spectral efficiency. To this end, we propose an alternating beamforming algorithm based on Neumann series expansion and the SCA optimization framework. Numerical results confirm the effectiveness and robustness of the proposed algorithms, benchmarked against state-of-the-art approaches. Overall, this work underscores the critical importance of MC-awareness in RIS-assisted channel estimation and beamforming, particularly in RIS configurations with high amplification and small inter-element spacing.

APPENDIX A PROOF OF PROPOSITION 1

Both functions, $f(\gamma)$ and $g(\gamma|\gamma_i)$, are a mapping: $\mathbb{C}^{N_I} \rightarrow \mathbb{R}$. Following the complex-value differentiation theory in [59], [61], we rewrite the two functions $f(\gamma)$ and $g(\gamma|\gamma_i)$ as $f(\gamma, \gamma^*)$ and $g(\gamma, \gamma^*|\gamma_i)$, respectively. Here, γ and γ^* are treated as two linearly independent variables.

According to (40) and (42), we have

$$g(\gamma, \gamma^*|\gamma_i) = -\gamma^H \mathbf{Q}_i \gamma + K(\gamma - \gamma_i)^H (\gamma - \gamma_i) - \gamma_i^H \mathbf{q} \gamma^T \mathbf{B} \gamma_i - \gamma_i^H \mathbf{B}^H \gamma^* \mathbf{q}^H \gamma_i - \gamma_i^H \mathbf{B}^H \gamma^* \gamma_i^T \mathbf{B} \gamma_i - \gamma_i^H \mathbf{B}^H \gamma_i^* \gamma^T \mathbf{B} \gamma_i. \quad (\text{A.1})$$

We can then observe that

$$\frac{\partial^2 g(\gamma, \gamma^*|\gamma_i)}{\partial \gamma \partial \gamma} = \frac{\partial^2 g(\gamma, \gamma^*|\gamma_i)}{\partial \gamma^* \partial \gamma^*} = \mathbf{0}, \quad (\text{A.2})$$

$$\frac{\partial^2 g(\gamma, \gamma^*|\gamma_i)}{\partial \gamma \partial \gamma^*} = \left(\frac{\partial^2 g(\gamma, \gamma^*|\gamma_i)}{\partial \gamma^* \partial \gamma} \right)^T = \mathbf{K} \mathbf{I} - \mathbf{Q}_i. \quad (\text{A.3})$$

Thus, the full complex Hessian matrix of $g(\gamma, \gamma^*|\gamma_i)$ is given by [55]

$$\mathbf{H}_i = \begin{bmatrix} (\mathbf{K} \mathbf{I} - \mathbf{Q}_i)^T & \mathbf{0} \\ \mathbf{0} & \mathbf{K} \mathbf{I} - \mathbf{Q}_i \end{bmatrix} \succeq \mathbf{0}. \quad (\text{A.4})$$

Here, the positive semi-definiteness of $\mathbf{H}_{\gamma, \gamma^*}$ is ensured by (41). Then, according to the second-order condition of convex functions [54, Sec. 3.1.4], $g(\gamma, \gamma^*|\gamma_i)$ is convex. Hence, Condition 1 in Section VI-A is satisfied.

Next, we derive the first-order derivatives of $f(\gamma, \gamma^*)$ and $g(\gamma, \gamma^*|\gamma_i)$ to assess whether they satisfy Condition 2. Based on (40), we can derive:

$$\frac{\partial f(\gamma, \gamma^*)}{\partial \gamma} = -(\gamma^H \mathbf{q}) \mathbf{q}^* - (\gamma^H \mathbf{q}) (\mathbf{B} + \mathbf{B}^T) \gamma - (\gamma^H \mathbf{B}^H \gamma^*) \mathbf{q}^* - (\gamma^H \mathbf{B}^H \gamma^*) (\mathbf{B} + \mathbf{B}^T) \gamma, \quad (\text{A.5})$$

$$\frac{\partial f(\gamma, \gamma^*)}{\partial \gamma^*} = -(\gamma^T \mathbf{q}^*) \mathbf{q} - (\gamma^T \mathbf{q}^*) (\mathbf{B}^H + \mathbf{B}^*) \gamma^* - (\gamma^T \mathbf{B} \gamma) \mathbf{q} - (\gamma^T \mathbf{B} \gamma) (\mathbf{B}^H + \mathbf{B}^*) \gamma^*, \quad (\text{A.6})$$

$$\frac{\partial g(\gamma, \gamma^*|\gamma_i)}{\partial \gamma} = -(\gamma^H \mathbf{q}) \mathbf{q}^* - (\gamma^H \mathbf{q}) \mathbf{B}^T \gamma_i - (\gamma^H \mathbf{B}^H \gamma_i^*) \mathbf{q}^* \quad (\text{A.7})$$

$$- (\gamma^H \mathbf{B}^H \gamma_i^*) \mathbf{B}^T \gamma_i + 2K(\gamma^* - \gamma_i^*) - (\gamma_i^H \mathbf{q}) \mathbf{B} \gamma_i - (\gamma_i^H \mathbf{B}^H \gamma_i^*) \mathbf{B} \gamma_i,$$

$$\frac{\partial g(\gamma, \gamma^*|\gamma_i)}{\partial \gamma^*} = -(\gamma^T \mathbf{q}^*) \mathbf{q} - (\gamma^T \mathbf{q}^*) \mathbf{B}^H \gamma_i - (\gamma_i^T \mathbf{B} \gamma) \mathbf{q} \quad (\text{A.8})$$

$$- (\gamma_i^T \mathbf{B} \gamma) \mathbf{B}^H \gamma_i^* + 2K(\gamma - \gamma_i) - (\gamma_i^T \mathbf{q}^*) \mathbf{B}^* \gamma_i^* - (\gamma_i^T \mathbf{B} \gamma_i) \mathbf{B}^* \gamma_i^*.$$

By comparing (A.5) and (A.7), we can see that $\frac{\partial f(\gamma, \gamma^*)}{\partial \gamma} |_{\gamma=\gamma_i} = \frac{\partial g(\gamma, \gamma^*|\gamma_i)}{\partial \gamma} |_{\gamma=\gamma_i}$. By comparing (A.6) and (A.8), we can see that $\frac{\partial f(\gamma, \gamma^*)}{\partial \gamma^*} |_{\gamma=\gamma_i} = \frac{\partial g(\gamma, \gamma^*|\gamma_i)}{\partial \gamma^*} |_{\gamma=\gamma_i}$. Thus Condition 2 in Section VI-A is satisfied, which concludes the proof.

REFERENCES

- [1] S. Kang *et al.*, "Cellular wireless networks in the upper mid-band," *IEEE Open J. of the Commun. Soc.*, vol. 5, pp. 2058–2075, 2024.
- [2] X. Wang *et al.*, "Millimeter wave communication: A comprehensive survey," *IEEE Commun. Surveys Tuts.*, vol. 20, no. 3, pp. 1616–1653, 2018.
- [3] T. S. Rappaport *et al.*, "Wireless communications and applications above 100 GHz: Opportunities and challenges for 6G and beyond," *IEEE Access*, vol. 7, pp. 78 729–78 757, 2019.

- [4] S. Tarboush *et al.*, “TeraMIMO: A channel simulator for wideband ultra-massive MIMO terahertz communications,” *IEEE Trans. Veh. Technol.*, vol. 70, no. 12, pp. 12 325–12 341, 2021.
- [5] M. Di Renzo *et al.*, “Smart radio environments empowered by reconfigurable intelligent surfaces: How it works, state of research, and the road ahead,” *IEEE J. Sel. Areas Commun.*, vol. 38, no. 11, pp. 2450–2525, 2020.
- [6] E. Björnson *et al.*, “Reconfigurable intelligent surfaces: A signal processing perspective with wireless applications,” *IEEE Signal Process. Mag.*, vol. 39, no. 2, pp. 135–158, 2022.
- [7] C. Pan *et al.*, “An overview of signal processing techniques for RIS/IRS-aided wireless systems,” *IEEE J. Sel. Topics Signal Process.*, vol. 16, no. 5, pp. 883–917, 2022.
- [8] K. Keykhosravi *et al.*, “Leveraging RIS-enabled smart signal propagation for solving infeasible localization problems: Scenarios, key research directions, and open challenges,” *IEEE Veh. Technol. Mag.*, vol. 18, no. 2, pp. 20–28, 2023.
- [9] H. V. Cheng and W. Yu, “Degree-of-freedom of modulating information in the phases of reconfigurable intelligent surface,” *IEEE Trans. Inf. Theory*, vol. 70, no. 1, pp. 170–188, 2024.
- [10] H. Chen *et al.*, “Multi-RIS-enabled 3D sidelink positioning,” *IEEE Trans. Wireless Commun.*, 2024, early access.
- [11] P. Zheng, X. Liu, and T. Y. Al-Naffouri, “LEO-and RIS-empowered user tracking: A Riemannian manifold approach,” *IEEE J. Sel. Areas Commun.*, 2024, accepted.
- [12] J. Rao *et al.*, “An active reconfigurable intelligent surface utilizing phase-reconfigurable reflection amplifiers,” *IEEE Trans. Microw. Theory Techn.*, vol. 71, no. 7, pp. 3189–3202, 2023.
- [13] Z. Zhang *et al.*, “Active RIS vs. passive RIS: Which will prevail in 6G?” *IEEE Trans. Commun.*, vol. 71, no. 3, pp. 1707–1725, 2022.
- [14] Z. Wan *et al.*, “Terahertz massive MIMO with holographic reconfigurable intelligent surfaces,” *IEEE Trans. Commun.*, vol. 69, no. 7, pp. 4732–4750, 2021.
- [15] T. Gong *et al.*, “Holographic MIMO communications: Theoretical foundations, enabling technologies, and future directions,” *IEEE Commun. Surveys Tuts.*, vol. 26, no. 1, pp. 196–257, 2024.
- [16] E. Björnson *et al.*, “Towards 6G MIMO: Massive spatial multiplexing, dense arrays, and interplay between electromagnetics and processing,” *arXiv preprint arXiv:2401.02844*, 2024.
- [17] G. Gradoni and M. Di Renzo, “End-to-end mutual coupling aware communication model for reconfigurable intelligent surfaces: An electromagnetic-compliant approach based on mutual impedances,” *IEEE Wireless Commun. Lett.*, vol. 10, no. 5, pp. 938–942, 2021.
- [18] P. Zheng, X. Ma, and T. Y. Al-Naffouri, “On the impact of mutual coupling on RIS-assisted channel estimation,” *IEEE Wireless Commun. Lett.*, vol. 13, no. 5, pp. 1275–1279, 2024.
- [19] P. Zheng *et al.*, “JrCUP: Joint RIS calibration and user positioning for 6G wireless systems,” *IEEE Trans. Wireless Commun.*, vol. 23, no. 6, pp. 6683–6698, 2024.
- [20] A. Rabault *et al.*, “On the tacit linearity assumption in common cascaded models of RIS-parametrized wireless channels,” *IEEE Trans. Wireless Commun.*, 2024, early access.
- [21] R. Faqiri *et al.*, “PhysFad: Physics-based end-to-end channel modeling of RIS-parametrized environments with adjustable fading,” *IEEE Trans. Wireless Commun.*, vol. 22, no. 1, pp. 580–595, 2023.
- [22] D. M. Pozar, *Microwave engineering*. John Wiley & sons, 2011.
- [23] M. T. Ivrlač and J. A. Nossek, “The multipoint communication theory,” *IEEE Circuits Syst. Mag.*, vol. 14, no. 3, pp. 27–44, 2014.
- [24] M. Nerini *et al.*, “A universal framework for multipoint network analysis of reconfigurable intelligent surfaces,” *IEEE Trans. Wireless Commun.*, 2024, early access.
- [25] H. Li *et al.*, “Beyond diagonal reconfigurable intelligent surfaces with mutual coupling: Modeling and optimization,” *IEEE Commun. Lett.*, vol. 28, no. 4, pp. 937–941, 2024.
- [26] A. Abrardo, A. Toccafondi, and M. Di Renzo, “Design of reconfigurable intelligent surfaces by using S-parameter multipoint network theory—optimization and full-wave validation,” *IEEE Trans. Wireless Commun.*, 2024, early access.
- [27] M. D. Renzo and M. D. Migliore, “Electromagnetic signal and information theory,” *IEEE BITS the Inf. Theory Mag.*, 2024, early access.
- [28] D. Wijekoon, A. Mezghani, and E. Hossain, “Phase shifter optimization in RIS-aided MIMO systems under multiple reflections,” *IEEE Trans. Wireless Commun.*, 2024, early access.
- [29] P. Zheng, R. Wang, A. Shamim, and T. Y. Al-Naffouri, “Mutual coupling in RIS-aided communication: Model training and experimental validation,” *IEEE Trans. Wireless Commun.*, 2024, early access.
- [30] P. Wang, J. Fang, H. Duan, and H. Li, “Compressed channel estimation for intelligent reflecting surface-assisted millimeter wave systems,” *IEEE Signal Process. Lett.*, vol. 27, pp. 905–909, 2020.
- [31] X. Wei, D. Shen, and L. Dai, “Channel estimation for RIS assisted wireless communications—Part II: An improved solution based on double-structured sparsity,” *IEEE Commun. Lett.*, vol. 25, no. 5, pp. 1403–1407, 2021.
- [32] J. Chen, Y.-C. Liang, H. V. Cheng, and W. Yu, “Channel estimation for reconfigurable intelligent surface aided multi-user mmWave MIMO systems,” *IEEE Trans. Wireless Commun.*, vol. 22, no. 10, pp. 6853–6869, 2023.
- [33] J. He, H. Wymeersch, and M. Juntti, “Channel estimation for RIS-aided mmwave MIMO systems via atomic norm minimization,” *IEEE Trans. Wireless Commun.*, vol. 20, no. 9, pp. 5786–5797, 2021.
- [34] K. Ardah, S. Gherekhloo, A. L. de Almeida, and M. Haardt, “TRICE: A channel estimation framework for RIS-aided millimeter-wave MIMO systems,” *IEEE Signal Process. Lett.*, vol. 28, pp. 513–517, 2021.
- [35] A. Ali, N. González-Prelcic, and R. W. Heath, “Millimeter wave beam-selection using out-of-band spatial information,” *IEEE Trans. Wireless Commun.*, vol. 17, no. 2, pp. 1038–1052, 2017.
- [36] S. Tarboush, A. Ali, and T. Y. Al-Naffouri, “Compressive estimation of near field channels for ultra massive-MIMO wideband THz systems,” in *Proc. IEEE Int. Conf. Acoustics, Speech, and Signal Process. (ICASSP)*, 2023, pp. 1–5.
- [37] —, “Cross-field channel estimation for ultra massive-MIMO THz systems,” *IEEE Trans. Wireless Commun.*, vol. 23, no. 8, pp. 8619–8635, 2024.
- [38] Q. Wu and R. Zhang, “Intelligent reflecting surface enhanced wireless network via joint active and passive beamforming,” *IEEE Trans. Wireless Commun.*, vol. 18, no. 11, pp. 5394–5409, 2019.
- [39] C. Huang *et al.*, “Reconfigurable intelligent surfaces for energy efficiency in wireless communication,” *IEEE Trans. Wireless Commun.*, vol. 18, no. 8, pp. 4157–4170, 2019.
- [40] R. Liu *et al.*, “Joint transmit waveform and passive beamforming design for RIS-aided DFRC systems,” *IEEE J. Sel. Topics Signal Process.*, vol. 16, no. 5, pp. 995–1010, 2022.
- [41] H. Li *et al.*, “Intelligent reflecting surface enhanced wideband MIMO-OFDM communications: From practical model to reflection optimization,” *IEEE Trans. Commun.*, vol. 69, no. 7, pp. 4807–4820, 2021.
- [42] X. Yu *et al.*, “Robust and secure wireless communications via intelligent reflecting surfaces,” *IEEE J. Sel. Areas Commun.*, vol. 38, no. 11, pp. 2637–2652, 2020.
- [43] Y. Chen *et al.*, “Enhancing the downlink rate fairness of low-resolution active RIS-aided signaling by closed-form expression-based iterative optimization,” *IEEE Trans. Veh. Technol.*, pp. 1–17, 2024.
- [44] Z. Peng *et al.*, “Beamforming optimization for active RIS-aided multiuser communications with hardware impairments,” *IEEE Trans. Wireless Commun.*, 2024, early access.
- [45] X. Qian and M. D. Renzo, “Mutual coupling and unit cell aware optimization for reconfigurable intelligent surfaces,” *IEEE Wireless Commun. Lett.*, vol. 10, no. 6, pp. 1183–1187, 2021.
- [46] A. Abrardo, D. Dardari, M. Di Renzo, and X. Qian, “MIMO interference channels assisted by reconfigurable intelligent surfaces: Mutual coupling aware sum-rate optimization based on a mutual impedance channel model,” *IEEE Wireless Commun. Lett.*, vol. 10, no. 12, pp. 2624–2628, 2021.
- [47] J. Lee, G.-T. Gil, and Y. H. Lee, “Channel estimation via orthogonal matching pursuit for hybrid MIMO systems in millimeter wave communications,” *IEEE Trans. Commun.*, vol. 64, no. 6, pp. 2370–2386, 2016.
- [48] R. Wang, Y. Yang, B. Makki, and A. Shamim, “A wideband reconfigurable intelligent surface for 5G millimeter-wave applications,” *IEEE Trans. Antennas Propag.*, 2024, early access.
- [49] R. Long, Y.-C. Liang, Y. Pei, and E. G. Larsson, “Active reconfigurable intelligent surface-aided wireless communications,” *IEEE Trans. Wireless Commun.*, vol. 20, no. 8, pp. 4962–4975, 2021.
- [50] S. Shen, B. Clerckx, and R. Murch, “Modeling and architecture design of reconfigurable intelligent surfaces using scattering parameter network analysis,” *IEEE Trans. Wireless Commun.*, vol. 21, no. 2, pp. 1229–1243, 2022.
- [51] R. Baraniuk, “A lecture on compressive sensing,” *IEEE Signal Process. Mag.*, vol. 24, no. 4, 2007.
- [52] E. Björnson, M. Bengtsson, and B. Ottersten, “Optimal multiuser transmit beamforming: A difficult problem with a simple solution structure [lecture notes],” *IEEE Signal Process. Mag.*, vol. 31, no. 4, pp. 142–148, 2014.

- [53] J. Liu, H. Li, and B. Himed, "Joint optimization of transmit and receive beamforming in active arrays," *IEEE Signal Process. Lett.*, vol. 21, no. 1, pp. 39–42, 2014.
- [54] S. P. Boyd and L. Vandenberghe, *Convex optimization*. Cambridge university press, 2004.
- [55] X.-D. Zhang, *Matrix analysis and applications*. Cambridge University Press, 2017.
- [56] J. M. Ortega, *Matrix theory: A second course*. Springer Science & Business Media, 2013.
- [57] G. Scutari *et al.*, "Decomposition by partial linearization: Parallel optimization of multi-agent systems," *IEEE Trans. Signal Process.*, vol. 62, no. 3, pp. 641–656, 2014.
- [58] A. Nedić *et al.*, "Parallel and distributed successive convex approximation methods for big-data optimization," *Multi-Agent Optimization: Cetraro, Italy 2014*, pp. 141–308, 2018.
- [59] A. Hjørungnes, *Complex-valued matrix derivatives: with applications in signal processing and communications*. Cambridge University Press, 2011.
- [60] O. El Ayach *et al.*, "Spatially sparse precoding in millimeter wave MIMO systems," *IEEE Trans. Wireless Commun.*, vol. 13, no. 3, pp. 1499–1513, 2014.
- [61] A. Hjørungnes and D. Gesbert, "Complex-valued matrix differentiation: Techniques and key results," *IEEE Trans. Signal Process.*, vol. 55, no. 6, pp. 2740–2746, 2007.